

AD-A068 185

HUGHES RESEARCH LABS MALIBU CALIF
CROSSED-FIELD CLOSING SWITCH DEVELOPMENT. (U)
APR 79 R HARVEY

F/G 9/1

UNCLASSIFIED

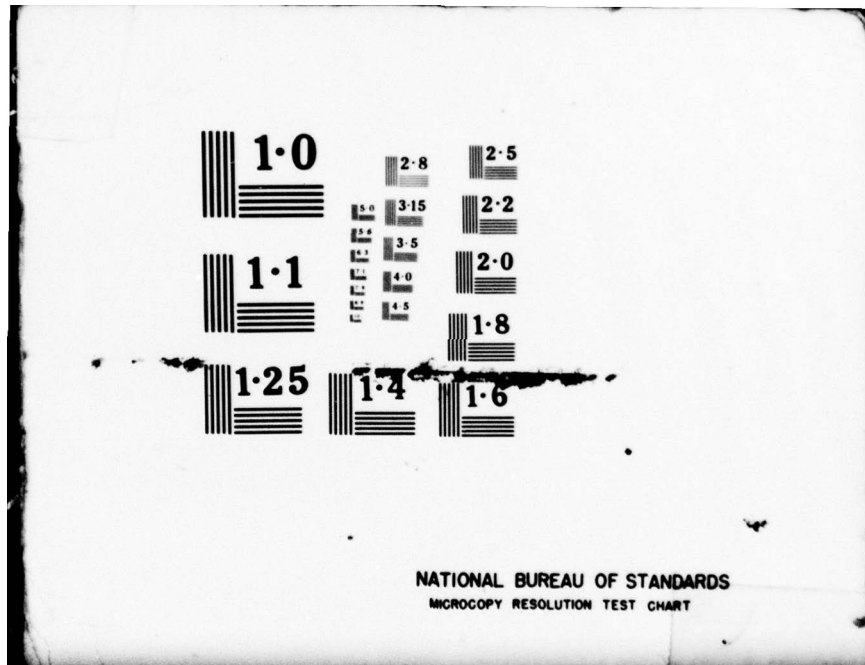
| OF |
ADA
068/85

DAABO
DELET-TR-77-2703-F

DAAB07-77-C-2703

NL

END
DATE
FILED
6-79
DDC





02
~~LEVEL~~

12
B.S.

Research and Development Technical Report
DELET-TR-77-2703-F

ADA068185

CROSSED FIELD CLOSING SWITCH DEVELOPMENT

DMC FILE COPY

Robin Harvey

Hughes Research Laboratories
3011 Malibu Canyon Road
Malibu, CA 90265

April 1979

Contract No. DAAB07-77-C-2703
Final Report
For period 29 July 1977 through 30 September 1978

Approved for public release; distribution unlimited.

Prepared for
Electronics Technology and Devices Laboratory
UNITED STATES ARMY ELECTRONICS
RESEARCH AND DEVELOPMENT COMMAND
Fort Monmouth, NJ 07703

ERADCOM

US ARMY ELECTRONICS RESEARCH AND DEVELOPMENT COMMAND
FORT MONMOUTH, NEW JERSEY 07703

095 02 008

HISA-FM 195-78

NOTICES

Disclaimers

The citation of trade names and names of manufacturers in this report is not to be construed as official Government indorsement or approval of commercial products or services referenced herein.

Disposition

Destroy this report when it is no longer needed. Do not return it to the originator.

UNCLASSIFIED

SECURITY CLASSIFICATION OF THIS PAGE (When Data Entered)

REPORT DOCUMENTATION PAGE		READ INSTRUCTIONS BEFORE COMPLETING FORM
1. REPORT NUMBER	2. GOVT ACCESSION NO.	3. RECIPIENT'S CATALOG NUMBER
4. TITLE (and Subtitle)		5. TYPE OF REPORT & PERIOD COVERED
6. CROSSED-FIELD CLOSING SWITCH DEVELOPMENT A065431		Final Report 29 July 1977-30 Sep 1978
7. AUTHOR(s)		8. CONTRACT OR GRANT NUMBER(s)
8. PERFORMING ORGANIZATION NAME AND ADDRESS Hughes Research Laboratories 3011 Malibu Canyon Road Malibu, California 90265		9. PROGRAM ELEMENT, PROJECT, TASK AREA & WORK UNIT NUMBERS 11162705AH 94 1702 9402GR
10. CONTROLLING OFFICE NAME AND ADDRESS UNITED STATES ARMY ELECTRONICS COMMAND FORT MONMOUTH, NEW JERSEY 07703		11. REPORT DATE April 1979
12. MONITORING AGENCY NAME & ADDRESS (if different from Controlling Office) ATTN: DELET-BG		13. NUMBER OF PAGES 67 12 59p
14. DISTRIBUTION STATEMENT (of this Report)		15. SECURITY CLASS. (of this report) UNCLASSIFIED
16. DISTRIBUTION STATEMENT (of the abstract entered in Block 20, if different from Report) 18. DELET		17. DECLASSIFICATION DOWNGRADING SCHEDULE
19. KEY WORDS (Continue on reverse side if necessary and identify by block number) High-power switches Plasma Crossed-field devices		
20. ABSTRACT (Continue on reverse side if necessary and identify by block number) The function of the crossed-field closing switch has been studied over a wide range of variables. It appears that the switch behavior is more complicated than originally expected. Three different modes of conduction have been observed: the conventional crossed-field discharge, a hybrid hollow-cathode discharge, and vacuum arcs. Depending on the amplitude and duration of the current, conduction may typically pass through these modes in the above sequence.		

DD FORM 1 JAN 73 1473 EDITION OF 1 NOV 68 IS OBSOLETE

UNCLASSIFIED

SECURITY CLASSIFICATION OF THIS PAGE (When Data Entered)

172 600

JOB

UNCLASSIFIED

SECURITY CLASSIFICATION OF THIS PAGE(When Data Entered)

The crossed-field closing switch may be triggered magnetically or by grid control into a number of states with varying levels of voltage drop. Conduction may be allowed in the reverse direction or prevented. The present design is limited in response speed and repetition rate by the inductance of the grid and anode leads, the lack of efficient pressure control, and the need for a pulsed magnetic field.

Criteria are presented which show the directions in which extrapolations in design may lead. It is concluded that the crossed-field closing switch is potentially capable of performing many functions more reliably or effectively than conventional switching devices, and variants of the device may eventually be capable of performing functions not presently achievable by any means.

UNCLASSIFIED

SECURITY CLASSIFICATION OF THIS PAGE(When Data Entered)

FOREWORD

The testing of the CFCS was performed at the USA Electronics Technology and Devices Laboratory at the Evans Area of Ft. Monmouth, N.J. in collaboration with Mr. John Creedon and his staff.

ACCESSION for	
NTIS	White Section <input checked="" type="checkbox"/>
DDC	Buff Section <input type="checkbox"/>
UNANNOUNCED	<input type="checkbox"/>
JUSTIFICATION	
BY	
DISTRIBUTION/AVAILABILITY DATES	
DIS	SP-5101
A	

79 05 02 938

TABLE OF CONTENTS

Section	Page
1 INTRODUCTION	7
2 EXPERIMENTAL PROGRAM	15
A. The CFCS	15
B. Experimental Tests	21
3 THEORETICAL ANALYSIS	51
A. Anode Fall Characteristics	51
4 SUMMARY AND DISCUSSION	59

SECTION 1

INTRODUCTION

The purpose of this program was to establish the basic limits and operating mechanisms of the crossed-field closing switch (CFCS). A water- and oil-cooled triode version of the switch was used in this work (Figure 1). It was built and demonstrated under an earlier program at an average power of 800 kW.¹ The present emphasis was on its high-speed response characteristics. Both the earlier and present operational limits are shown in Table 1.

Basically, the CFCS is a low-pressure gas discharge device with concentric electrodes.^{2,3,4} It is first put into a ready state by pulsing a magnetic field in the axial direction, and then triggered into conduction by raising the grid electrode voltage up from cathode potential. Conduction is initiated between the cathode and the grid in the form of a classical crossed field discharge (XFD). One of several mechanisms then causes plasma to pass through the grid into the anode-grid gap and close the circuit. An outline of the basic mechanisms is given in Table 2.

The experimental program was begun by repairing the grid feedthrough bushings (which had been damaged the year before) and by replacing a faulty automatic He leak valve with a manually operated one. The switch was then shipped back to the ERADCOM high-power test facility at the Evans area of Fort Monmouth, New Jersey. Data was subsequently taken during roughly six travel periods of about one week each.

The first tests were aimed at reestablishing the earlier operational levels. Although we were able to achieve operation at 8 Hz, 47 kV, and 50 kA peak current, it became quite evident that the tube's behavior had degraded markedly; the principal symptoms were unstable triggering, flashovers at the grid leads, and uncharacteristic

8208-20

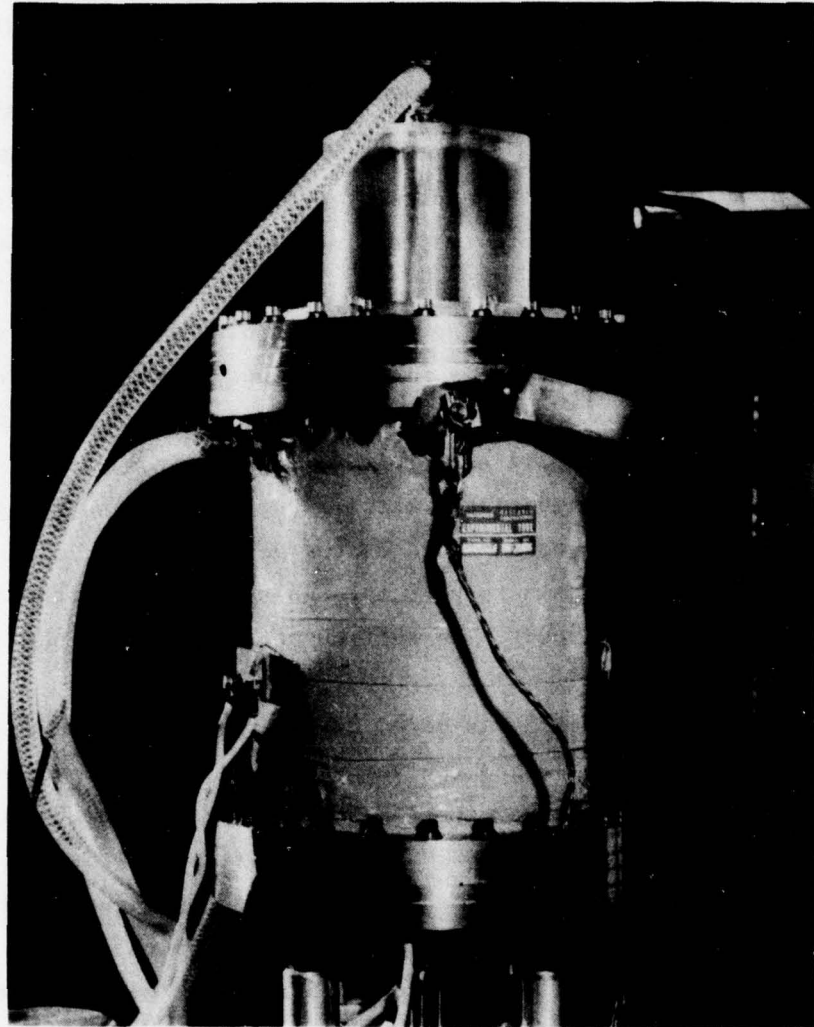


Figure 1. The crossed-field closing switch (CFCS-T-4).

Table 1. Operational Limits

Parameter	Previous Limits ^a	New Limits
Current, kA	40	50
Voltage, kV	40	47
Rise time, μ sec	1	0.050
Jitter, μ sec	0.1	0.010
Pulse width, μ sec	10	0.170
Repetition, rate, Hz	80	1327
Average current, A	40	
Average power, kW	800	

^aSimultaneous operation.

6463

kickouts. The causes can now be traced to an array of circumstances, including a lack of alignment of the grid following repair, a spurious change in the auxiliary trigger output levels, the lack of automatic pressure control, changes in the test circuit, ground-loop falsification of undesirable tube function, and an inability to independently adjust the grid trigger pulse time.

The most important electrical characteristics were found to be the system inductance, the grid trigger pulse timing relative to the magnetic field pulse, and the amplitude of the magnetic field. Small variations in other system parameters, such as gas pressure and voltage, may be accommodated by tuning the grid timing and the field strength. The lack of good pressure control resulted in trigger stability problems; but even so, once the auxiliary pulsers were replaced by more flexible circuits, the switch was again operated at 800 kW for 30 sec.

Once we gained confidence in its performance, the tube was installed in a low-impedance (1 to 2 Ω) test circuit consisting of a parallel cable pulse forming network (PFN), a low-inductance water

Table 2. Basic Mechanisms

Conduction Phase	Mechanism
Grid-cathode trigger	Crossed-field discharge starts. Preionizes anode-grid gap.
Dwell time	Statistical time lag reduced. Anode-grid voltage reduced by plasma leakage and increase in grid voltage thereby reducing magnetic field requirement for crossed-field discharge in anode-grid gap.
Anode fall	Crossed-field discharge forms in anode grid gap; time scale depends on pressure, magnetic field, and voltage. Grid voltage rises, slowing down anode fall; magnetic field must be high enough to keep grid in conduction or tube drop will be high.
Transfer to hollow-cathode mode	Grid and anode voltages drop to low level with conduction in hybrid hollow cathode mode.
Glow to arc transition	Arc on one or more electrodes reduces voltage further.
Extinction and recovery	Current will continue to flow until power source is exhausted and/or magnetic field is removed. Recovery is by normal rapid magnetic interruption or by vacuum arc recovery.

6463

resistor, and a low-inductance header (Figure 2). Many of the features experienced with longer pulses became more obvious. By carefully adjusting the various parameters, a repetition rate of over 1300 Hz was achieved at 20 kV and 5.4 kA. We found that the anode fall time can be reduced to the apparent circuit-limited fall time of 50 nsec by increasing the pressure. By contrast, trigger stability can be improved by lowering the pressure (as can the Paschen breakdown hold-off voltage). High-power runs were not made above 25 kV with the low-inductance header because of recurrent insulating oil contamination. By extrapolating from present data, it appears that increasing the voltage would force a longer anode fall time.

The initial anode current couples strongly to the grid, driving the grid voltage upward. The amplitude of the grid voltage spike is directly related to the initial trigger timing, and a high grid voltage is coincident with high anode voltage drop. Control of the grid voltage

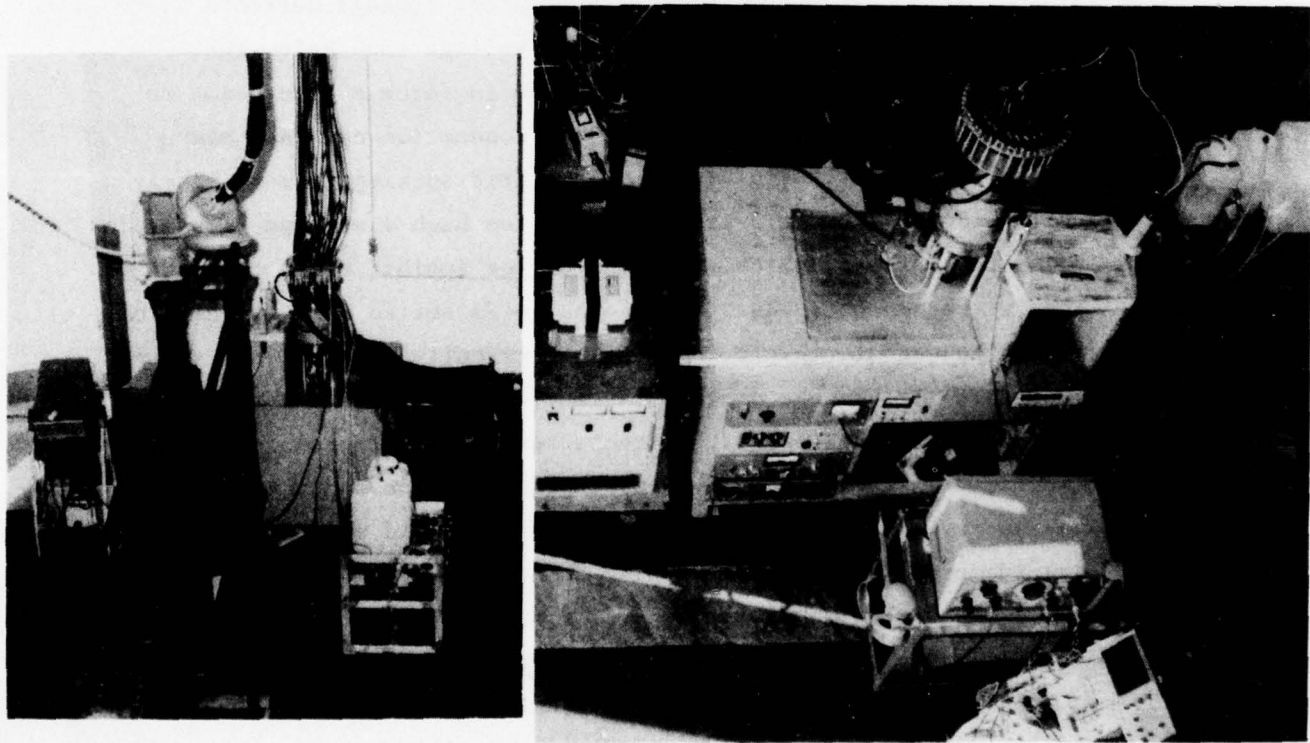


Figure 2. Experimental arrangement at ERADCOM.

spike was attempted by changing the trigger circuit, but the relatively high grid lead-in inductance negated these attempts.

At a low anode voltage, the switch can be made to conduct in either a hollow-cathode glow-discharge mode (with a conduction voltage drop of about 180 V) or in an XFD mode (at roughly 400 V). The transition from the crossed-field mode to the hollow-cathode mode appears to occur after the conduction of a given amount of charge. The hollow-cathode conduction voltage drop is consistent with earlier thermal measurements of the tube voltage drop. This probably is the basic mechanism for the conduction of high currents when an arc is not present and when the grid voltage is low.

Operationally, the effect of the grid pulse, at low system inductance, is to reduce the statistical and formative time lags (and thus the jitter) of the anode current relative to the magnetic field pulse. This presumably is because the grid discharge provides a high level of pre-ionization. At a high enough system inductance, leakage currents from the grid-cathode space will pull the anode voltage down below the critical starting level ($V_c \sim B^2$) long enough to force a transition to an XFD in the anode-grid gap. Thus, anode conduction can take place at a relatively low magnetic field. Since grid spiking is more likely at such low fields, the grid may end up at too high a voltage to sustain the XFD to the cathode, which would cut off or inhibit anode conduction.

The switch conducts when the grid pulse is set to fire at the minimum sustaining magnetic field, even if the circuit inductance is small. This is assumed to be caused by the formation of ions in the grid-cathode gap with relatively high directed energies. Increasing the magnetic field slightly actually stops the anode from conducting. Although not well understood, this low magnetic field mode of operation may have important advantages for high-repetition-rate operation.

The anode fall time is expected from first principles to have a component inversely proportional to the pressure. This is observed over a limited pressure range. But at about 50 mTorr of He, a very

slow precursory fall begins prior to the expected rapid fall. As the pressure is reduced, the slow fall is extended. This seems to be related to the anomalous voltage fall observed in diode CFCSs.⁵

When the pressure is increased, the current and voltage pulse waveforms approach a limiting trapezoidal shape, with the apparent intrinsic anode fall time tracking the theoretical prediction down to 10 nsec at 120 mTorr. This same trapezoidal shape is evident in control pulses made at low voltage using a low-inductance mechanical switch located across the tube anode and ground leads within the HV header.

The switch's conduction voltage is a function of the magnetic field. At high field, it runs in either polarity with a low voltage drop. As the field is reduced, conduction is first cut off in the reverse direction and then impeded by a rising voltage drop in the forward direction. This voltage drop variation may be explained by the known conduction properties of the individual gaps (anode-grid and grid-cathode).

On the basis of this work, new criteria have been established for the design of future CFCS systems. The CFCS is potentially capable of performing many functions more reliably or effectively than conventional switching devices. Variants of the new switch may eventually be capable of performing functions not presently achievable by any means.

SECTION 2
EXPERIMENTAL PROGRAM

A. The CFCS

1. Earlier Work

The CFCS is based on early work by Makinson¹ and by Boucher.² The first diode version of the CFCS was developed at Hughes Research Laboratories (HRL) as a spinoff from crossed-field interrupters.^{3,4,5} Later, a grid electrode was added by Lutz^{6,7,8} to reduce the magnetic field requirements and to allow a more classical grid control of the discharge. (Similar work has been done independently by Vishnewskii⁹ and by Soldatenko,¹⁰ who typically report switching power levels well below those considered here.)

A prototype high-average-power triode CFCS (Figure 3) was built under contract with the U.S. Army Electronics Command (Contract No. DAAB07-76-C1313).¹¹ The original goals of that program were 40 kV, 20 kA at 125 Hz with a rise time of 1 μ sec, and a pulse width of 10 μ sec. The device was tested successfully to 800 kW of average power, the maximum limit then possible at the ECOM facility (40 kV, 40 kA, and 80 Hz). The results are shown in Table 1. The relationship of the operating voltage to the helium pressure is shown qualitatively in Figure 4. The expected normal operating region is bounded at high pressure by Paschen breakdown and at low pressure by the anomalous ignition characteristic of XFDs at high voltage.¹² The upper voltage limit is given by vacuum breakdown between electrodes or across the feedthrough bushing. The lower voltage limit is set by loss of grid control. That is, the magnetic field pre-triggers an XFD at the anode whenever

$$V \gtrsim \frac{ed^2 B^2}{2M}, \quad (1)$$

M11666

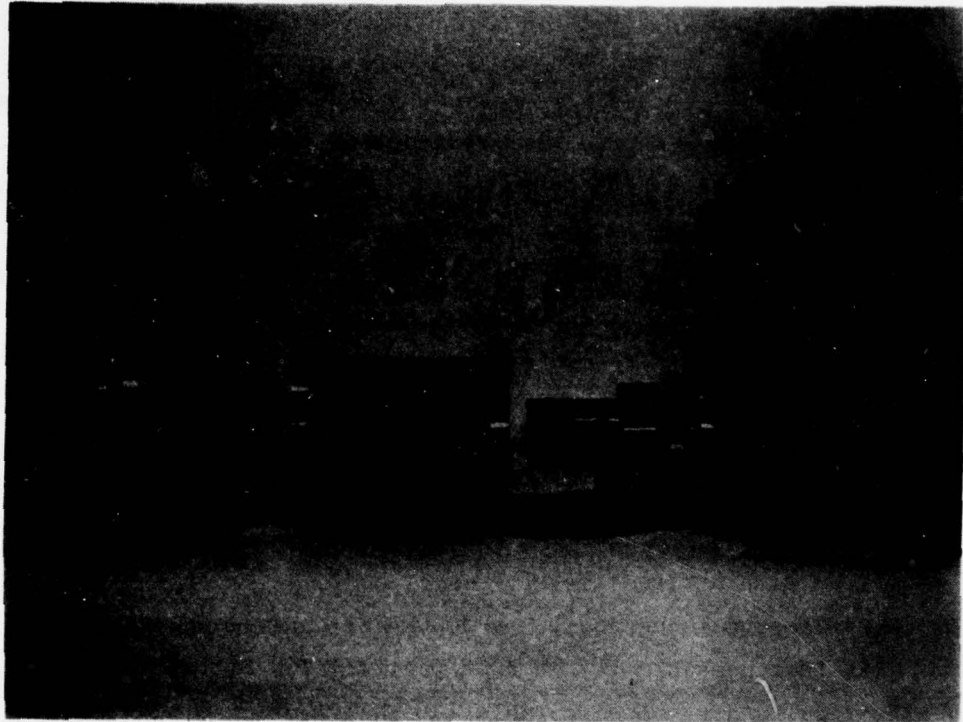


Figure 3. Assembly view of CFCS T-4.

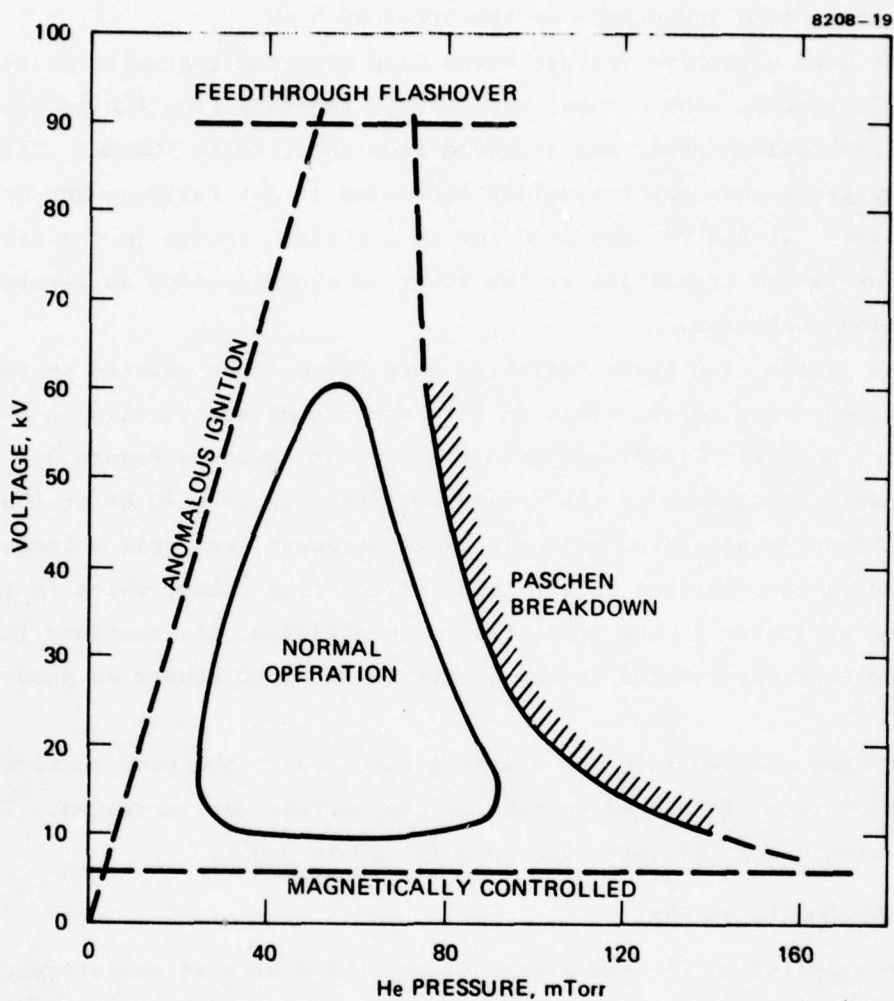


Figure 4. Normal operating range of CFCS.

where d is the distance to the grid, and M is the electron mass. This picture of the normal operating range is qualitatively correct for circuits with a lead inductance on the order of $5 \mu\text{H}$.

The mean effective voltage drops were measured thermally at the three electrodes. The cathode drop varied smoothly from 400 to 115 V as the peak switch power was increased from about 20 to 800 MW. This range suggests that the conduction mechanism is not fully an XFD or a vacuum arc. It can be accounted for by a gradual change in the timing of a glow-to-arc transition as the power is changed or by an alternative conduction mechanism.

The jitter time characteristics were found to be related to the grid current time delay. This in turn depends parametrically on the pressure, magnetic field, and grid voltage, as shown in Figure 5. The curves were obtained with the device switching on from 40 kV at 120 Hz. Fluctuations in pressure, magnetic field strength, and grid voltage resulted in fluctuations in the grid current time delay, which in turn appeared as jitter in the anode fall. In addition, fluctuations in the anode voltage contributed to the jitter in the same manner as diode CFCSSs.⁵

The gas cleanup rate was a strong function of the peak current and repetition rate; it seemed to fall as the current was increased. The interpretation of this pressure data is now in doubt.

2. Tube Modifications

In preparation for the present work, the source of an intermittent vacuum leak was discovered to be at a grid feedthrough bushing. These grid leads are shown in a cutaway drawing of the tube in Figure 6. Two of the four are hollow, for coolant flow, and the others are solid rods. The Kovar seals of the four grid feedthrough bushings were found to have been weakened by the presence of corrosive residue inadvertently trapped there during initial cleaning of the tube. Rust spots were also found on nearby cathode surfaces. This indicates that mechanical vibrations

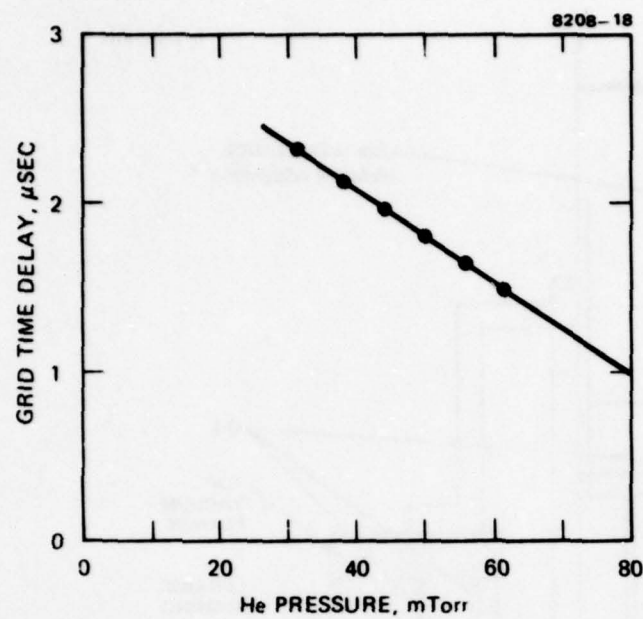
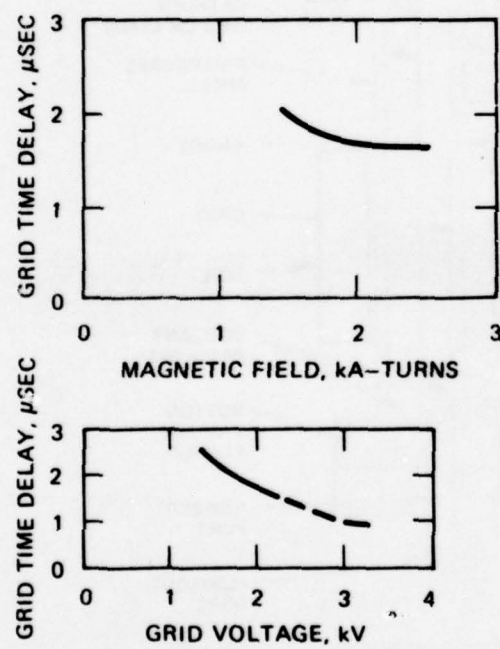


Figure 5.
Parametric dependences
of grid delay.



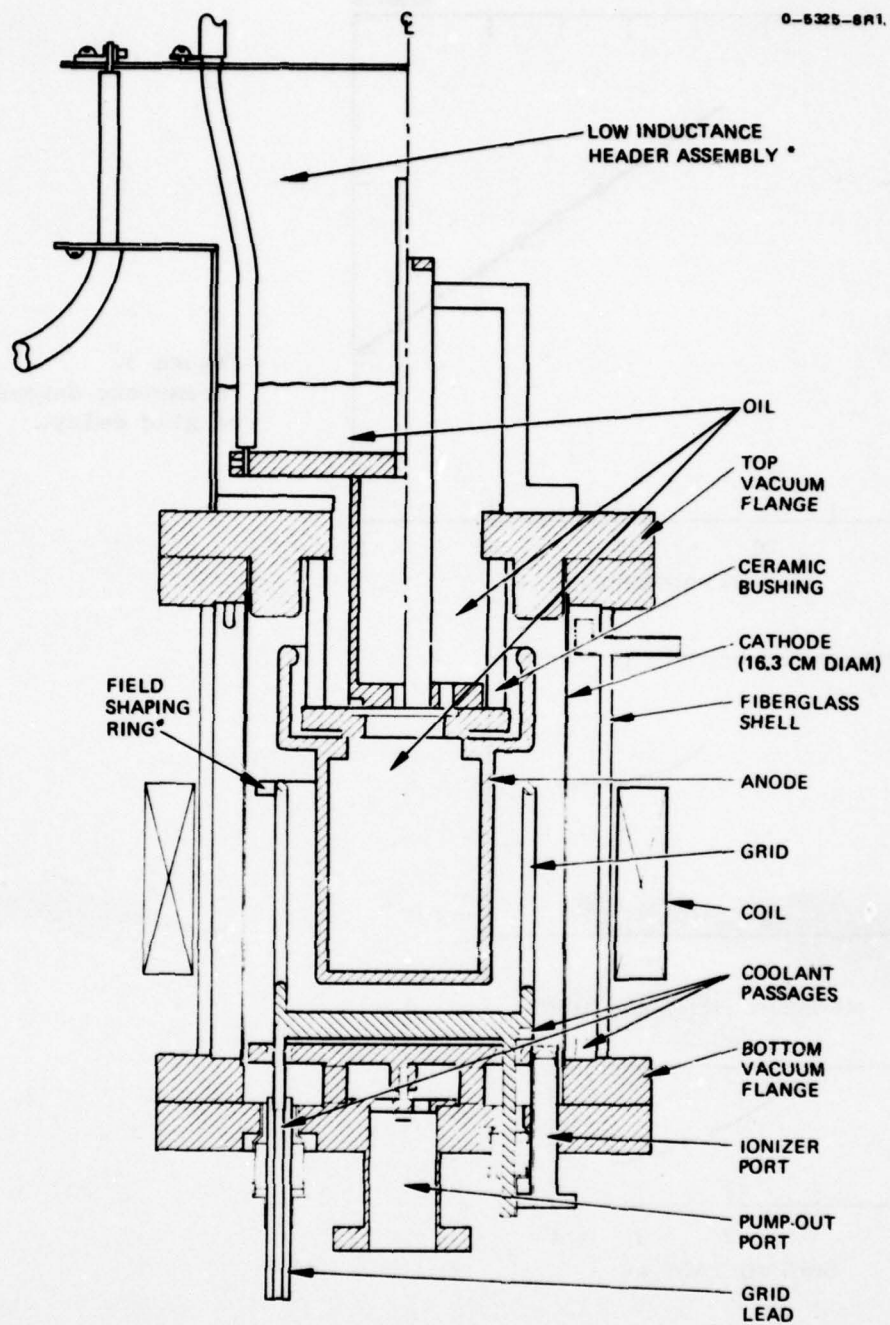


Figure 6. Cutaway drawing of CFCS.

* Denotes later changes.

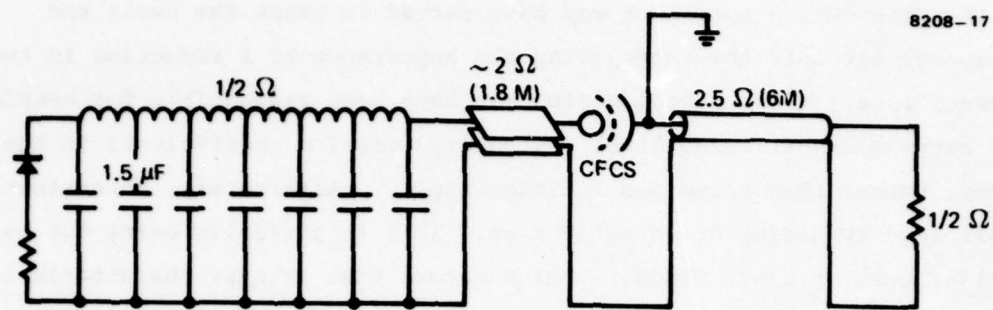
of the grid during operation may have served to crack the seals and introduce air into the tube, giving the appearance of a reduction in the cleanup rate. Also, contamination may have been responsible for keeping the cathode conditioning level (secondary emission coefficient) in the normal rather than anomalous ignition region. Alternately, contamination would lead to arcing at an early time. This is partially borne out by earlier work on diode CFCSSs,¹² which showed that trigger characteristics into the crossed-field glow are degraded with extended conditioning.

The tube was repaired by replacing the grid bushings and removing the oxides from the electrodes. Later alterations (left side of Figure 6) included adjusting the grid alignment by changing the length of the support rods, adding a field shaping ring at the top of the grid, and installing a low-inductance header for use with a cable pulse forming network (PFN). The calculated lead inductance of the header and cables down to the anode collector plate is 12 nH. The calculated inductance of the remainder of the switch (excluding the plasma) is 28 nH, yielding a total of 40 nH of lead inductance compared to about 100 nH without the header. The tube and header capacitance is calculated to be 77 pF without oil in the header and 135 pF with oil.

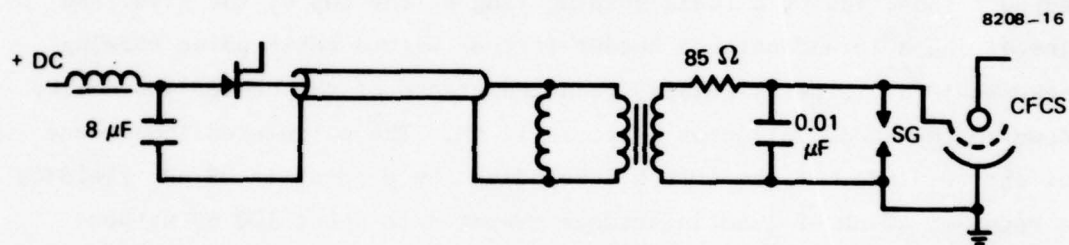
B. EXPERIMENTAL TESTS

1. Initial Tests

Initially, the tube was installed in a test circuit (Figure 7) using a $\frac{1}{2} \Omega$ PFN and a matched water load.¹³ The circuit was similar to that used the previous year, and the auxiliary pulsers were the same. However, the performance of the tube was qualitatively different. Initially, the tube behaved much as it had previously. Then, as the tube was aged by conditioning, conduction became unstable and was sometimes characterized by a high grid voltage and by a substantial noise modulation on the anode current pulse signal (Figure 8).



(a) PFN and LOAD test circuit



(b) Grid pulser

Figure 7. Low frequency test circuit.

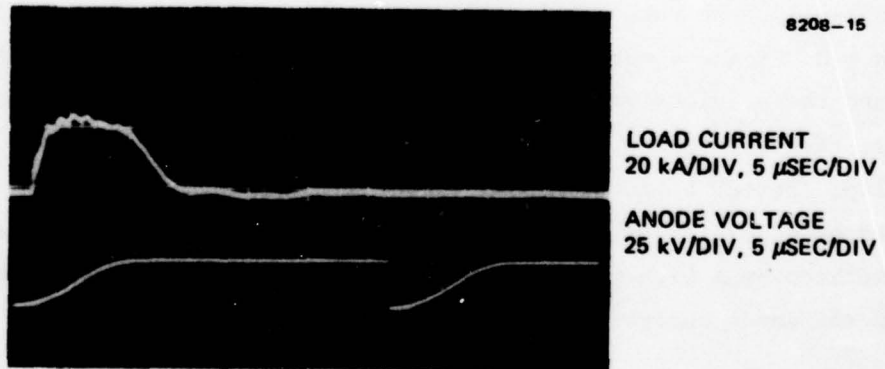


Figure 8. Current waveform in initial 1/2-Ω circuit.

The unstable operation was related to a noticeably high gas cleanup rate, and the original auxiliary control settings for the magnetic field and grid drives were no longer satisfactory. The ideal operating point appeared to be beyond the range of the original units.

The tube was run at 11.5 Hz for over 5 min at 47 kV with a peak current of 50 kA, but erratic triggering, external flashovers at the grid leads, and kickouts (continuous conduction) were commonly observed on other runs. Additional capacitance across the grid had little effect on the tube behavior other than to protect the bushings from flashover by holding the voltage spike down.

The presence of impurities in the gas fill was observed following several runs by noting that the pumpout rate of the ion pump on the vacuum station was markedly higher than expected for pure He. Since the calibrations of the millitorr and DV36 thermocouple vacuum gauges depend on the gas composition, the absolute pressure was not well known. (Control of these impurities was attempted using a Ti sublimation pump, but the pump never functioned properly.) A careful examination of the Paschen curve using fresh He revealed that the turn-on characteristics were displaced to the right of the turn-off characteristics by about 10% (Figure 9). (This suggests a hollow-cathode mode of conduction.) Furthermore, the turn-on point at 40 kV was at a considerably lower pressure than indicated by the previous data (56 mTorr rather than 84 mTorr).

Figure 10 shows the normal grid characteristics with no voltage on the anode. The top trace is the grid current inverted. The lower trace is the voltage at the peaking capacitor (0.01 μ F in Figure 7(b)). The capacitor is pulse charged to the desired voltage (about 2 kV) and then is automatically discharged into the grid when the latter conducts. The grid cuts off when the capacitor voltage rings negative and then restarts as the capacitor recharges. Low-level conduction continues at about 250 V, presumably in an XFD. Figure 11 shows the grid response

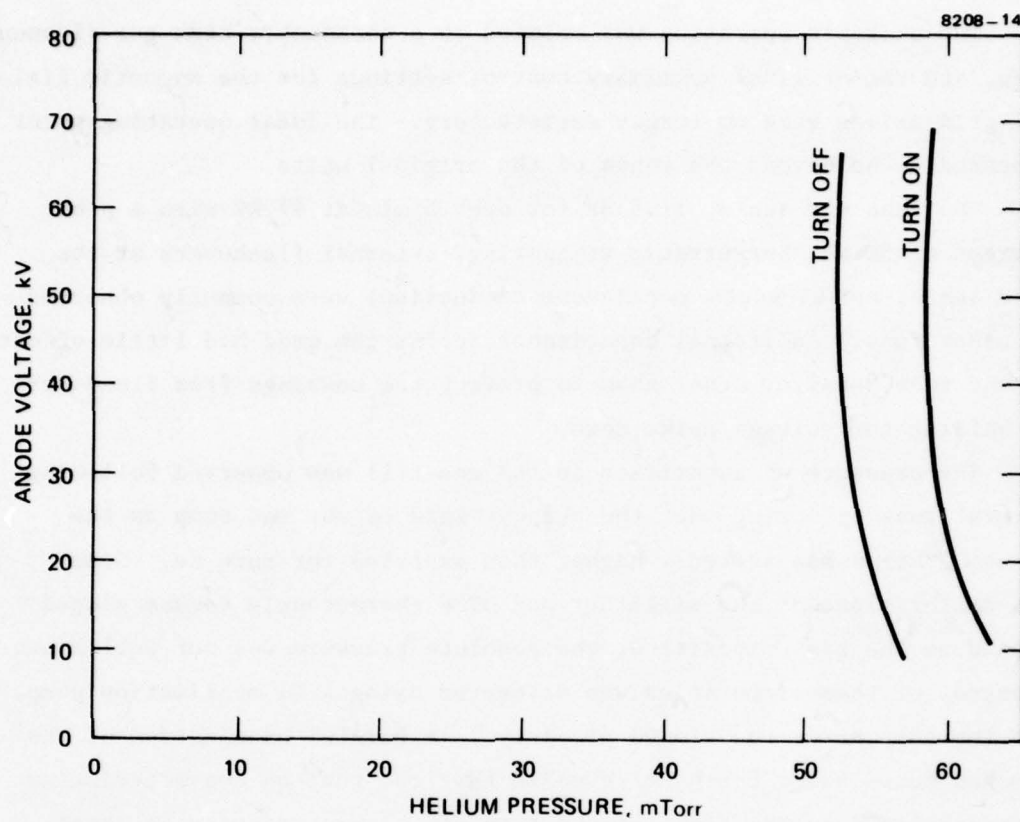


Figure 9. Paschen curve with grid misalignment.

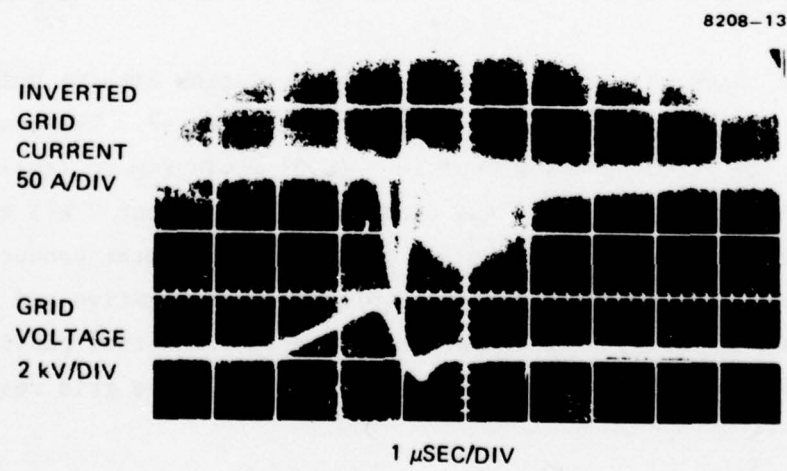


Figure 10. Grid pulse shape with peaking capacitor.

8208-12

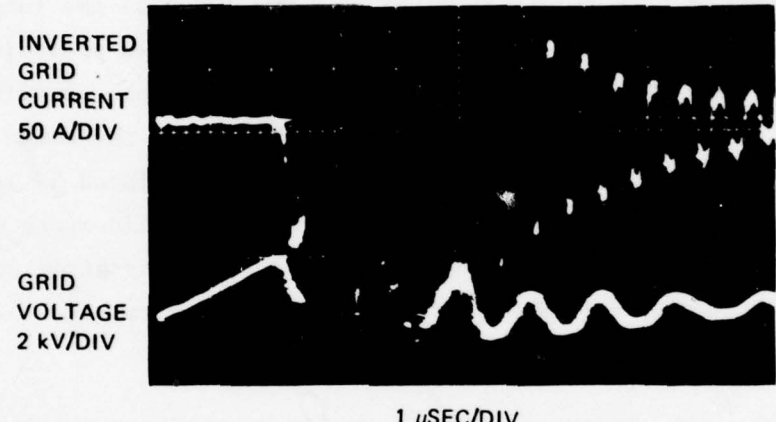


Figure 11. Grid response to anode conduction.

when the anode is charged to 22 kV. Here, a positive jump in the grid voltage at the start of anode conduction causes the protective spark gap to fire and excites a violent resonant excitation in the grid trigger circuit.

The SCR grid trigger circuit was eventually destroyed by the high-voltage noise coupling, and it was replaced by a remotely located thyratron and $1-\Omega$ PFN (Figure 12). The grid signals without the peaking capacitor are shown in Figure 13. Ground loops in the long lead cables coupled strongly to the remainder of the system producing the resonant 1-mHz noise visible in Figure 14. A principle contribution to the noise generation was the strip line used between the anode and the PFN. The noise level and resonances could be manipulated by introducing inductance at various points in the circuit. The solid-state magnetic field pulser was also replaced by a more versatile thyratron system with a variable pulse width and larger peak current rating.

2. Grid and Anode Ignition Characteristics

The ignition characteristics of an XFD in the grid and anode region differ due to the slight radial dependence of the magnetic field and to the physical shadowing of the anode region from the preionizer source. The effect of the reduction in preionization is to increase the jitter of the anode when triggered magnetically. Once this is taken into account, it is possible to measure the maximum starting voltage of either the grid or anode as a function of the magnetic field. In Figure 15, the curve labeled G-K was made with the anode floating and the grid held at a fixed voltage. The anode response A-G was made with the grid grounded. The difference between the two is due to the radial dependence of the magnetic field.

In Figure 16, these curves are replotted to show the on-state characteristics as a function of the grid voltage and magnetic field. Obviously, it is possible for the grid to be at a level where

8208-11

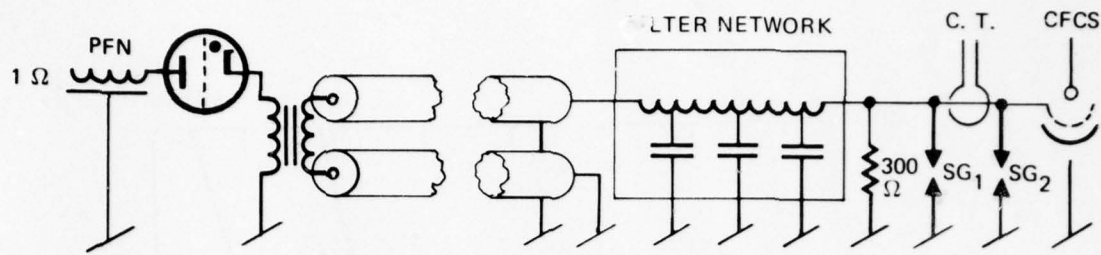


Figure 12. Remote grid drive circuit.

7452-4

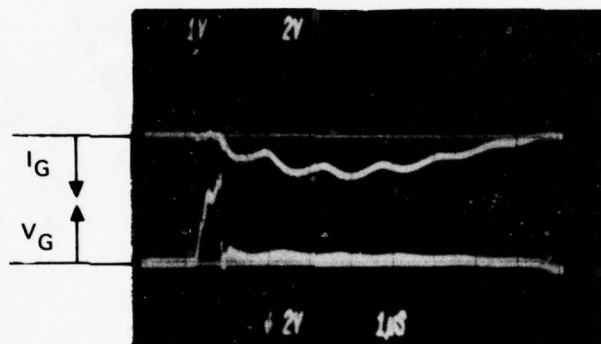


Figure 13. Grid pulse waveforms.

8208-10

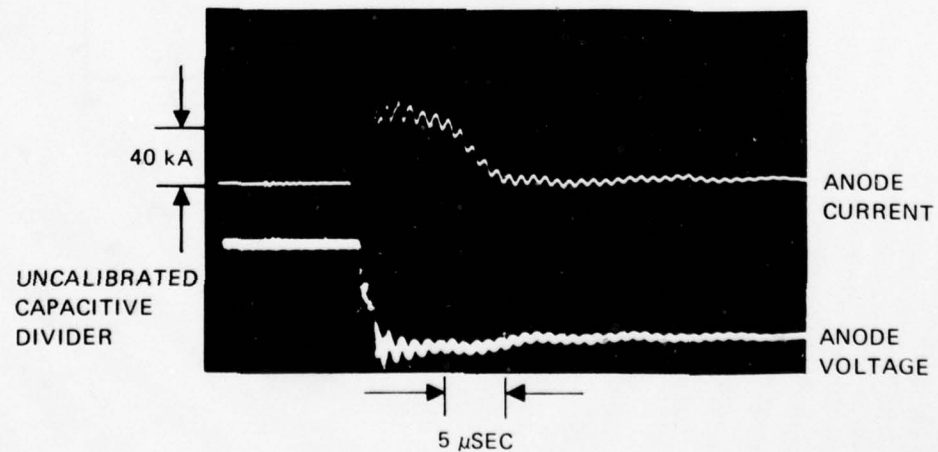


Figure 14. Grid ground long interaction with anode current signal.

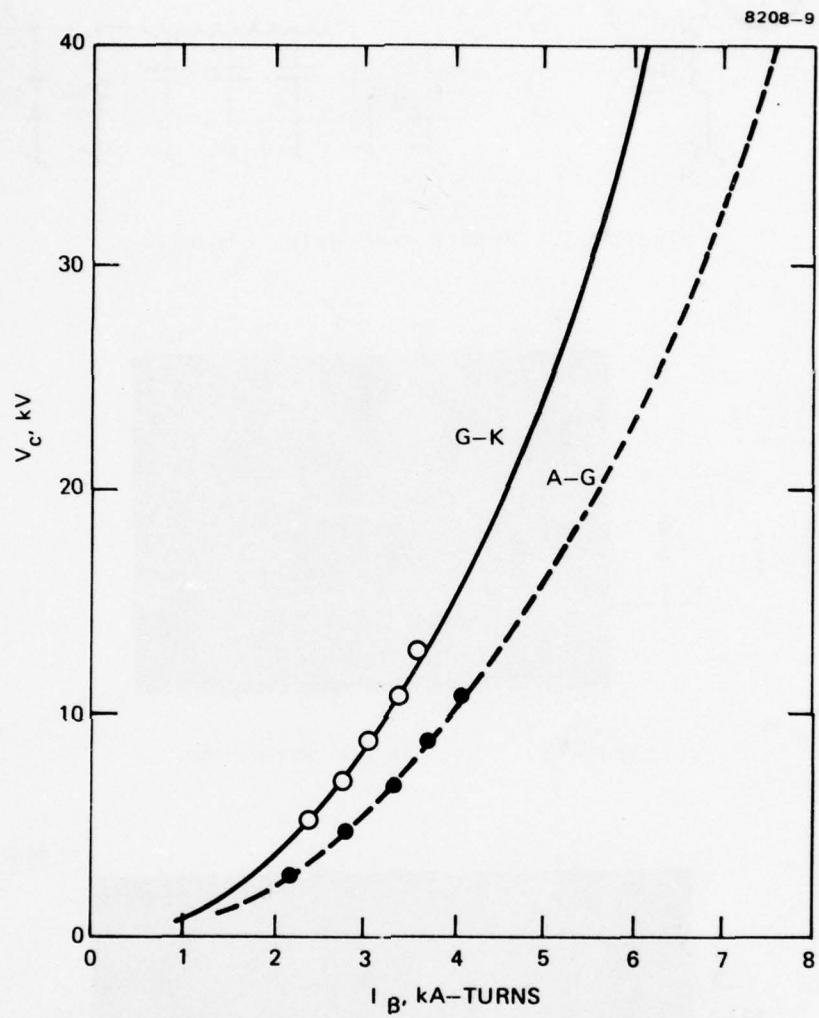


Figure 15. Grid and anode magnetic ignition characteristics.

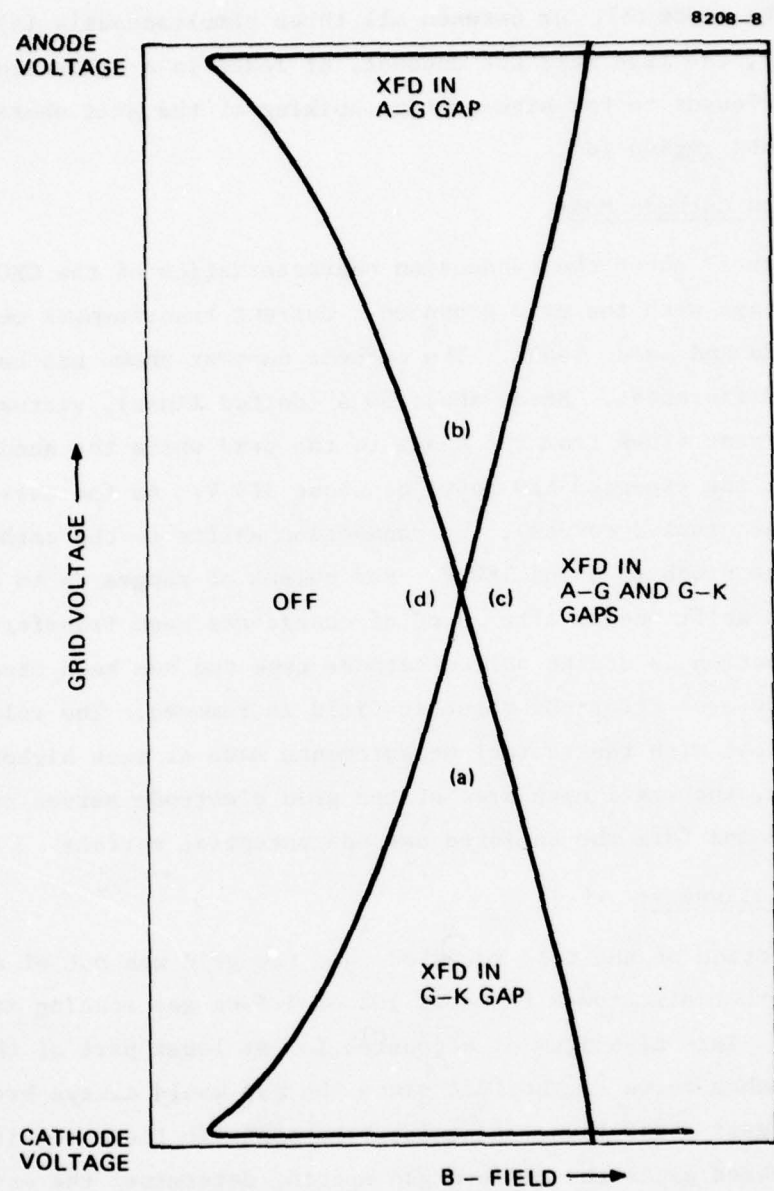


Figure 16. Schematic of simultaneous magnetic ignition characteristics.

conduction will take place between it and the cathode (a), between the grid and the anode (b), or between all three simultaneously (c). In region (d), the tube will not conduct, at least in a conventional XFD. This is relevant to the high-voltage spiking of the grid where it may jump up into region (d).

3. Hollow Cathode Mode

Figure 17 shows the conduction characteristics of the CFCS at low anode voltage with the grid grounded. Current transformers were placed in the grid and anode leads. The cathode current shown was computed from the differences. Below about 50 A (dotted lines), virtually all of the current flows from the anode to the grid while the anode voltage remains at the expected XFD level of about 310 V. As the current level is increased (solid curves), the conduction shifts to the cathode and the voltage drops to about 180 V. For pulses of ranges up to about 100 A, the shift occurs after 3 mC of charge has been transferred. Such conduction is of the hollow-cathode type and has been observed^{7,8} to continue even after the magnetic field is removed. The voltage drop is consistent with the thermal measurements made at much higher currents. Presumably, the small open area of the grid electrode serves to trap the plasma and form the enclosed cathode potential surface.

4. Grid Alignment

Inspection of the tube revealed that the grid was out of alignment with the other electrodes by about 10% of 1.5-cm gap spacing at the upper end. This misalignment accounted for at least part of the shift of the Paschen curve to the left since the gap would always break down at its largest separation. Likewise, the magnetic field requirements were increased since the minimum gap spacing determines the maximum electron orbit size for trapping. Taken together with the effects of the asymmetry on the electron drift, this also accounted for the observed reduction in the growth rate of the plasma. The grid was realigned at the test site and the original Paschen curve reestablished.

8208-7

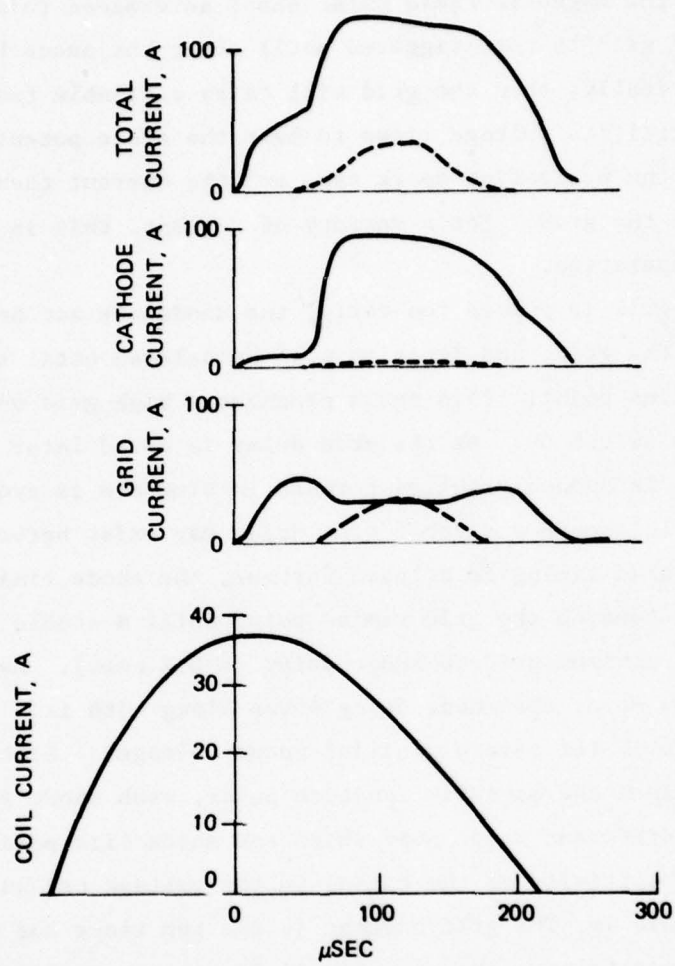


Figure 17. Low-voltage operation with grid grounded to cathode.

5. Anode and Grid Pulling

The relative timing of the grid pulse to the normal magnetic (XFD) ignition point of the anode is a critical parameter in the functioning of the tube. The magnetic field pulse shape determines this ignition point. If the grid is not triggered until after the anode has been started magnetically, then the grid will carry a sizable fraction of the current until its voltage rises to near the anode potential. This over-voltages the protection spark gap, and the current then flows to ground through the grid. For a variety of reasons, this is an undesirable mode of operation.

When the grid is pulsed too early, the anode may not be put into conduction by the grid, and ignition will be delayed until the normal magnetic ignition point. This again produces a high grid voltage when the anode does switch on. As the grid delay is moved later in time, the anode fall is suddenly pulled forward in time and is synchronized with the grid (although a sizable time delay may exist between the two). As the grid timing is delayed further, the anode timing moves slowly forward towards the grid timing point until a stable point is reached with a minimum grid-to-anode delay ($\sim 0.2 \mu\text{sec}$). As the grid is delayed even more, the anode delay moves along with it. This is shown in Figure 18 for several initial anode voltages. Since the voltage determines the magnetic ignition point, each anode voltage setting has a different range over which the anode fire point can be pulled. The sensitivity of the timing to the voltage can be seen more clearly in Figure 19. The grid current is the top trace and the anode current the lower trace. The magnetic field was set to fire the anode at a maximum of about 18 kV. Figure 19(a) was made at the stable operating voltage for a fixed grid timing. As the anode voltage increased slightly, the anode timing began to shift and to become unstable.

8208-6

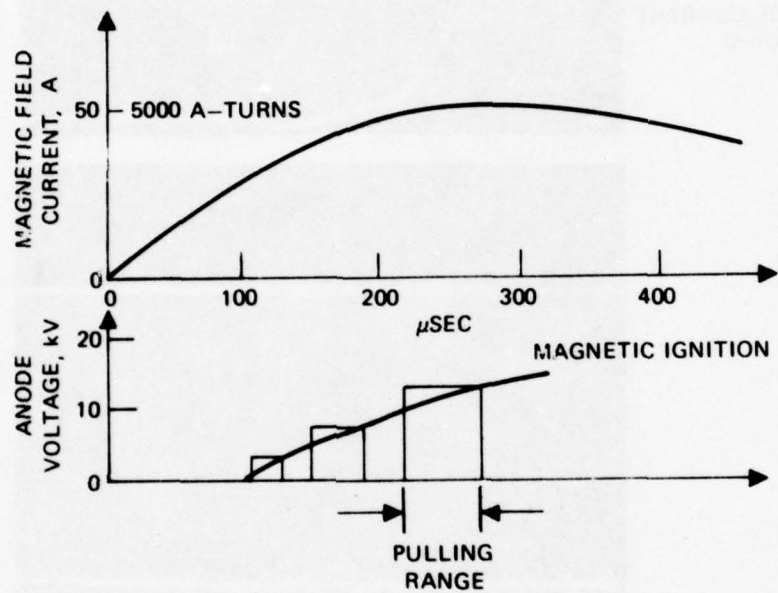


Figure 18. Anode pulling.

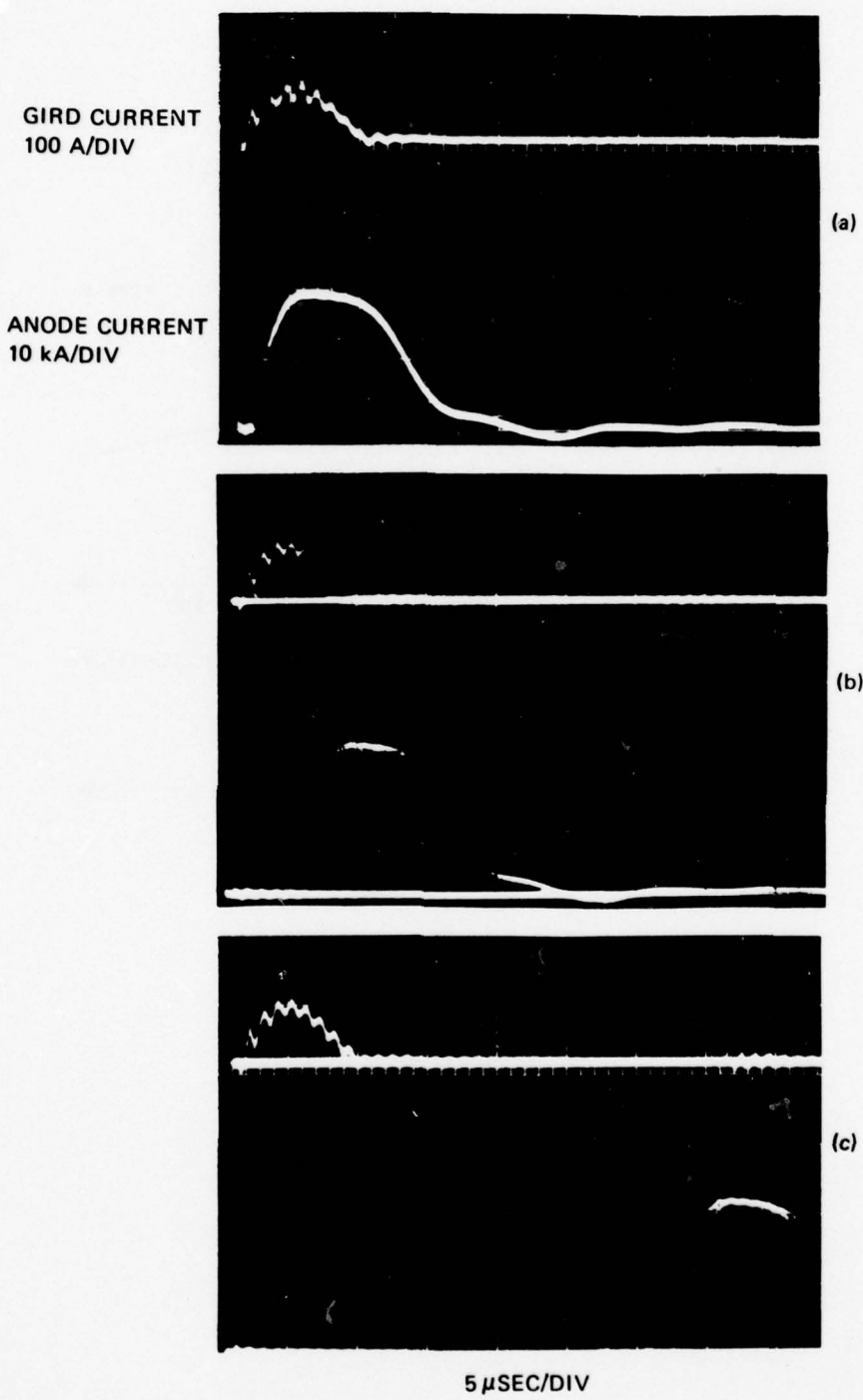


Figure 19. Anode pulse delay with increasing voltage.

The pulling range is also sensitive to the pressure. At 5 kV, the anode timing was pulled 20 μ sec at about 55 mTorr but as much as 100 μ sec at 36 mTorr. This variation is attributed to longer statistical and formative times in the growth of the plasma at low pressure and to variations in the magnetic ignition characteristics, due to less efficient utilization of energetic electrons at low pressure.⁴

Figure 20 shows an additional anomaly detected during the last phases of testing with the cable PFN system. This figure was made by reducing data such as that shown in Figure 21. Here, the anode delay is plotted as a function of the grid delay. With a fixed anode voltage and magnetic field pulse shape, the magnetic trigger point is at 80 μ sec; it is shaded to indicate the extent of the jitter. Stable grid triggered operation is obtained at about 60 μ sec. If the grid delay is moved either forward or backward, the anode trigger reverts to the magnetic control. At about 37 μ sec, the grid is at its earliest magnetically triggered point and the grid pulse amplitude is reduced to zero for earlier times. Just at this point, the anode fires. The mechanism is not known but may involve a difference in energetics of the plasma in the grid section at minimal magnetic field. With the exception of this anomalous trigger mechanism, all of the other trigger mechanisms appear to be tractable by utilizing the known XFD ignition characteristics.

6. 800-kW Operation

After the grid was realigned, the tube behavior improved. Beginning at low frequency and low voltage, the average switched power was increased continuously to 800 kW (40 kV, 40 A average) and held there for about 30 sec. During the run, the magnetic field current had to be increased continuously to 110 A, and the grid timing was continuously adjusted to the stable point. The pressure gauge failed early in the run, and the resulting pressure variations are not known.

On the basis of this run, we concluded that proper control of all the critical parameters would allow stable high-power operation. These

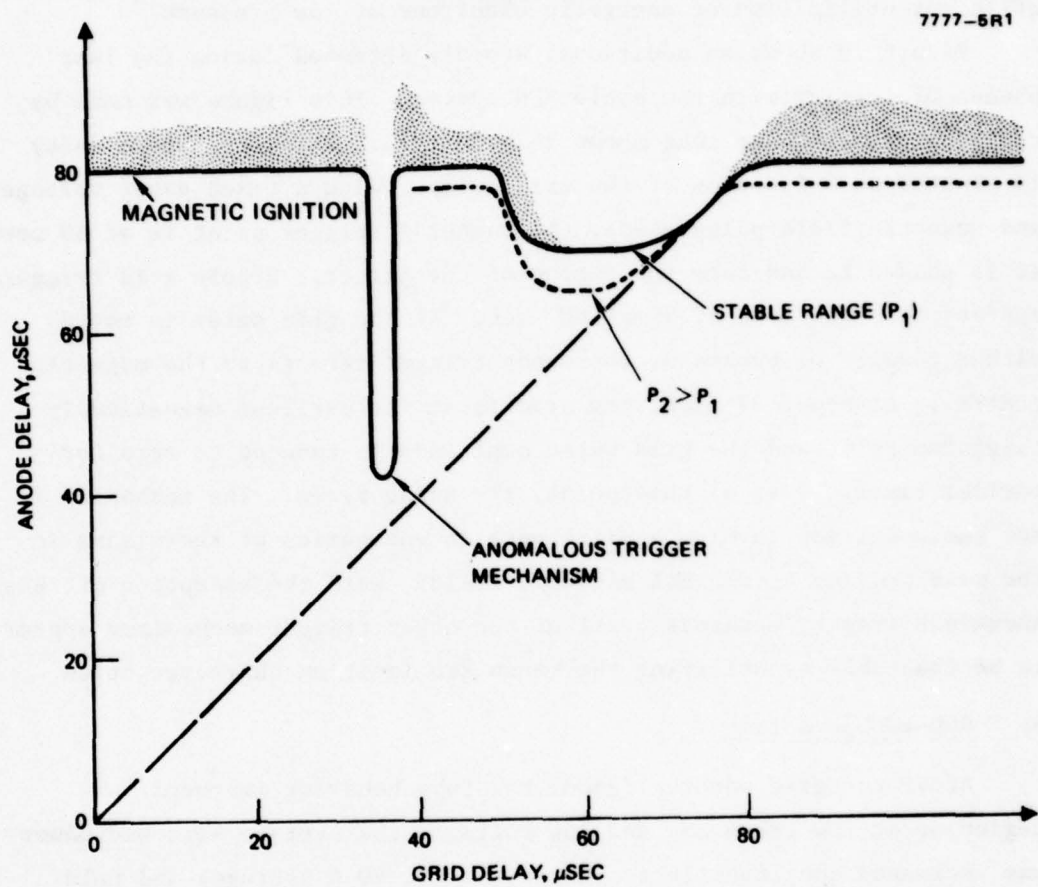


Figure 20. Anode time delay with grid trigger delay.

7777-8R1

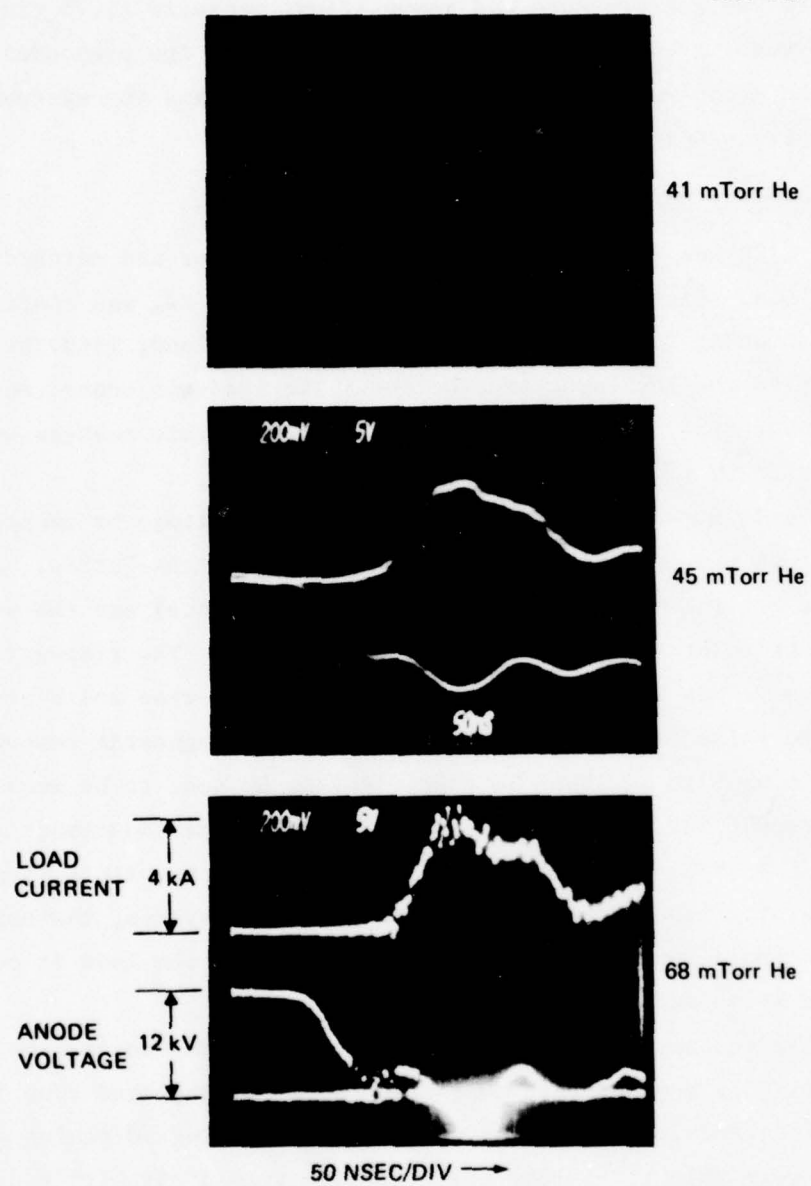


Figure 21. Approach of switch to inductively limited response with increasing pressure.

parameters are gas pressure and composition, magnetic field rise time and amplitude, grid trigger timing and amplitude, the preionization level, the anode voltage, the system inductance, and the system resonant frequencies.

7. High-Frequency Test Circuit

The CFCS was evaluated using a cable modulator and matched copper sulfate load. First the system impedance, Figure 22, was configured to be 2Ω using 25 RG214/U cables, each 15.24 m long, with the PFN connected to the low inductance header. The load was connected by an equal number of 4.57-m-long cables. Later, the cable numbers were increased to 50 to yield a 1Ω system.

The system response was calibrated at low voltage by mechanically shorting out the CFCS at point A with a low-inductance strap. Figure 23 shows the current measured at the anode (lower trace) and the voltage measured at point B (upper trace) at 50 nsec/div. The trapezoidal current pulse has a characteristic linear 40 nsec rise and a similar fall. The pulse width is about 175 nsec. The diagnostic response time is thought to be about 10 nsec, leaving 30 nsec to be accounted for by circuit inductance. For such a network, the inductance is given by $L = 2R \cdot \Delta t = 120 \text{ nH}$. This is an order of magnitude larger than the calculated header inductance.* With the 1Ω system, the expected rise time would increase somewhat; by shorting out the load it could be increased by an additional factor of two.

High-frequency noise at about 70 MHz is evident during the pulse rise time. This resonance is consistent with the expected tube internal ringing frequency. By shorting the load and ringing 50 cables with the CFCS, we were able to measure the effective lumped circuit inductance to be 67 nH (taking the cable capacitance to be $0.077 \mu\text{F}$).

* The experimental header inductance is consistent with measurements made using a thyratron in place of the CFCS. (Private communication with John Creedon.)

7452-1R1

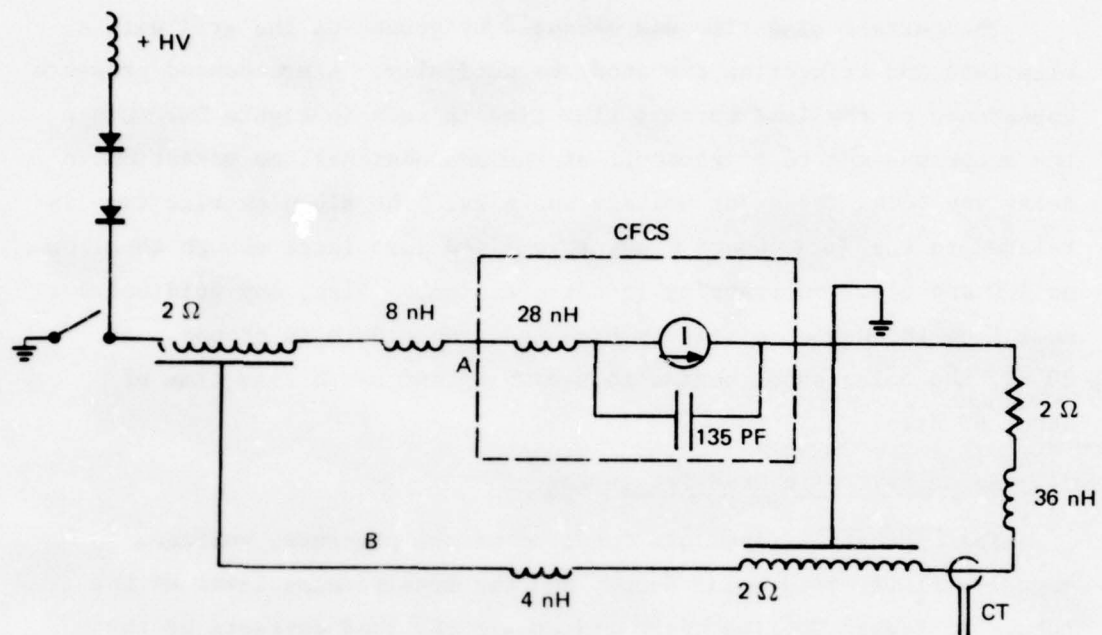


Figure 22. Cable test circuit.

7452-2R1

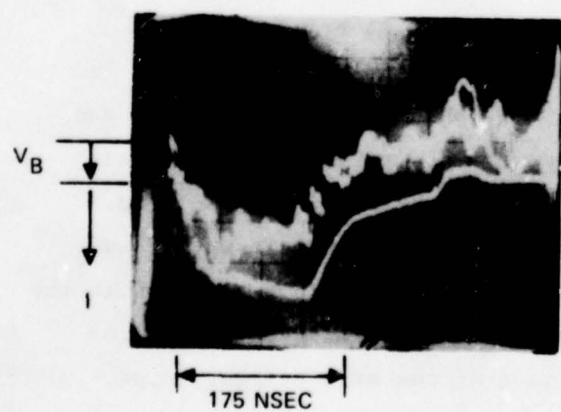


Figure 23.
System calibration
pulse.

8. Current Rise Time With Magnetic Triggering

The current rise time was measured by grounding the grid with a clip lead and triggering the anode magnetically. A pronounced pressure dependence on the load current rise time is seen in Figure 24. Since the scope was set to trigger off of the anode signal, no variation in delay was seen. The anode voltage was 6 kV. The sluggish rise time is related to the fact that a magnetic field just large enough to allow an XFD and electron trapping is not efficient. Also, any grid current must flow through a relatively high inductance path to ground. At 20 kV, the pulse shape begins to square up and has a rise time of about 60 nsec.

9. Anode Fall with Grid Triggering

The anode fall time is a function of the pressure, voltage, magnetic field, grid pulse shape, and the conditioning level of the tube. In Figure 25, the upper traces are the load currents at three different pressure settings with an anode voltage of 12 kV. In all cases, the current rises more or less exponentially until it reaches the linear portion of the rise. As the pressure is increased, the exponential rate increases until that portion of the curve is barely perceptible at 68 mTorr. At this pressure, the front of the pulse rise approaches the shape of the calibration waveforms. At higher pressure (see Figure 26) the exponential part of the signal disappears in the noise altogether, and the pulse shape is trapezoidal.

The grid waveform is correlated to the anode fall waveform and to the magnetic field strength. Figure 27 shows the anode current and grid voltage at two different delay settings relative to the rising magnetic field. The PFN was configured to be 1Ω , and the load cables were shorted out at the CFCS. The anode voltage was 12 kV. The current was measured by integrating a pick-up loop signal with the loop located in the header section. When the timing is early, the grid voltage rises slowly at the onset of the grid trigger pulse. At

8208-4

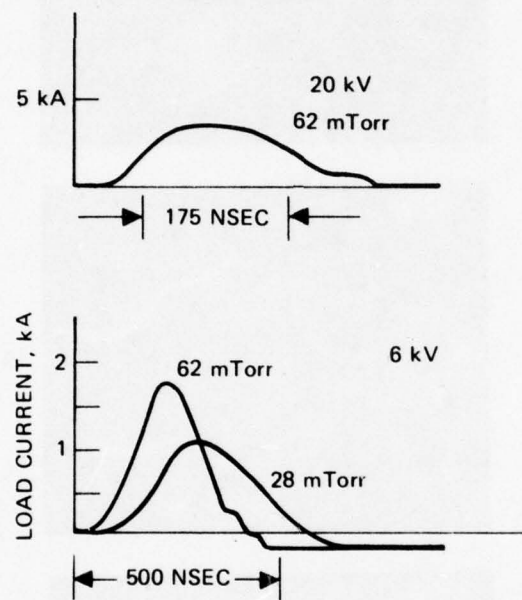


Figure 24. Anode current rise with magnetic triggering.

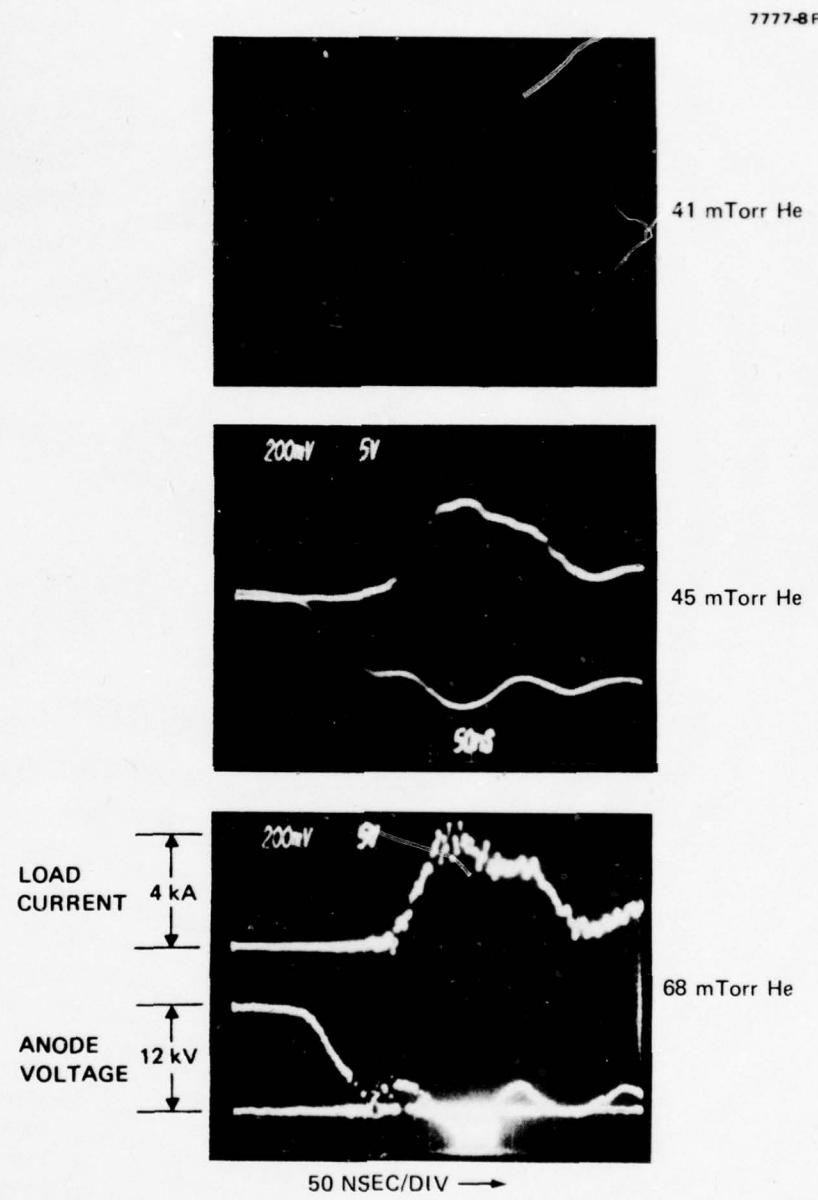


Figure 25. Approach of switch to inductively limited response with increasing pressure.

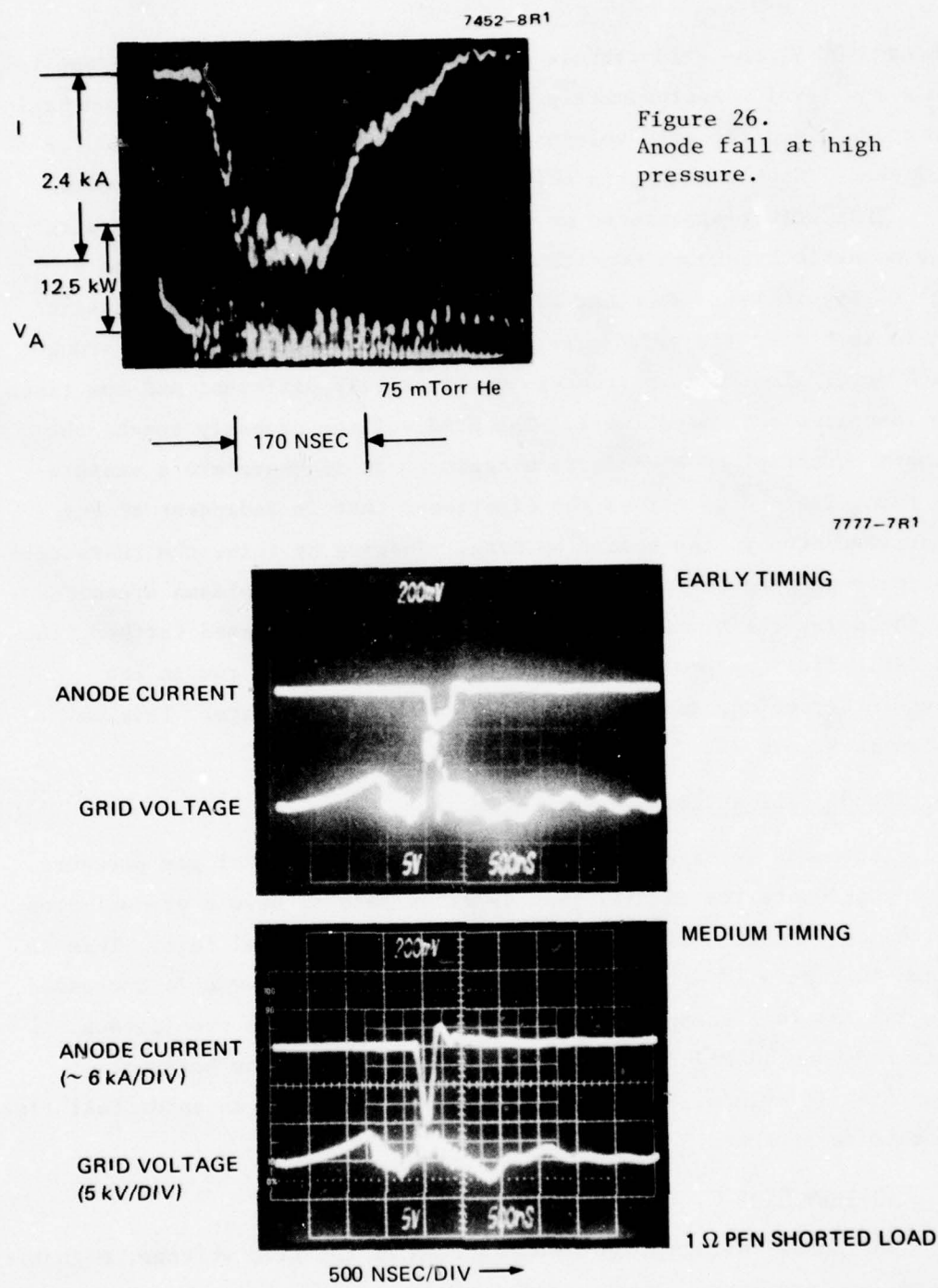


Figure 27. Effect of grid voltage on anode current.

about 3500 V, the grid-cathode section breaks down and the voltage falls to a low level. Approximately 0.5 μ sec later, the anode section begins to conduct and the grid voltage jumps up to 8 kV, where it holds for 0.2 μ sec. Such a high grid voltage retards the growth of current.

This effect appears to be caused by the grid voltage exceeding the magnetic breakdown conditions (i.e., the operating point is at (b) of Figure 16). When the timing is delayed so that the magnetic field is higher, the grid spike rises as before but is quickly brought back down. The anode current is qualitatively different and now rises to the circuit-limited level. The grid voltage probably tracks the plasma potential once conduction begins. It is therefore a measure of the voltage drop across the electrodes that is independent of any inductive drop in the header bushing. Judging by this, the characteristic 50-nsec anode fall time is not related to the plasma dynamics. As the delay relative to the magnetic field is increased further, the magnetic field becomes high enough to allow an XFD to run in the reverse direction, and the resulting anode signal rings. This is shown in Figure 28.

10. Anode Fall at Low Pressure

The anode voltage fall appears to be a function of gas pressure. At low pressure, the initial fall is often seen to have a gradual drop in the beginning, followed by a more rapid exponential fall. This is shown in Figure 29 at 37 mTorr of He. When the pressure is increased, the initial fall component disappears and the drop is precipitous. This is shown in Figure 30 at 50 mTorr. (Noise in the horizontal amplifier is evident, negating any attempt to assign an anode fall time at this sweep speed.)

11. Voltage Drop

The anode voltage drop is a function of the grid voltage, magnetic field, and pressure. Under optimal conditions, such as those observed

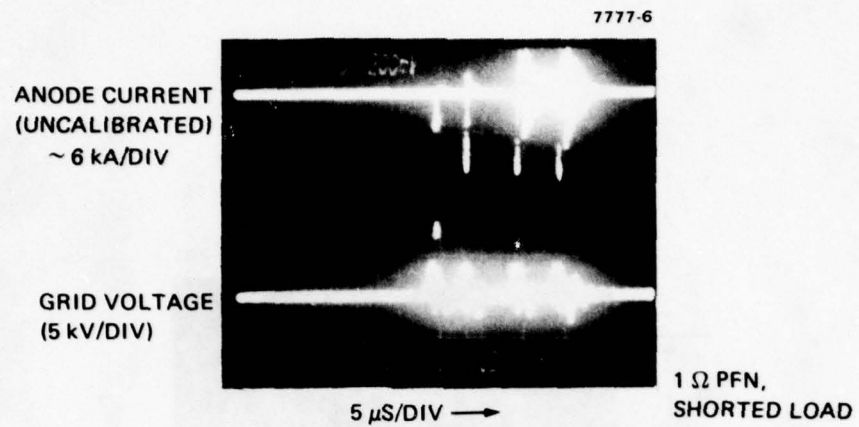


Figure 28. Variation of tube impedance with delay.

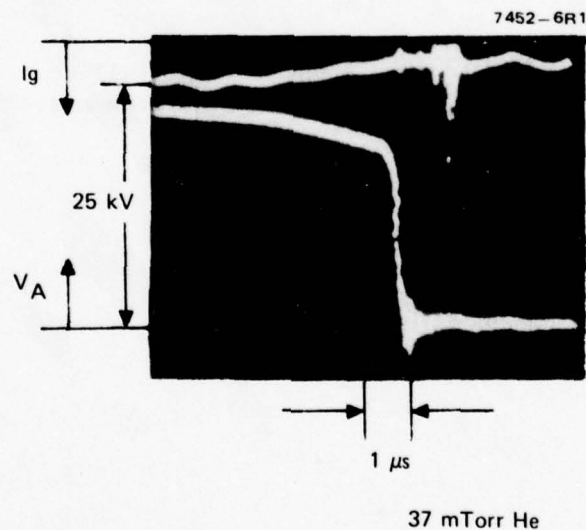


Figure 29. Anode voltage fall at low pressure.

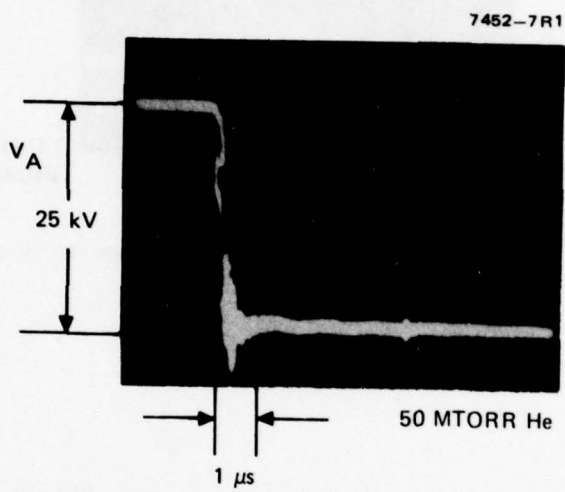


Figure 30. Anode voltage fall at intermediate pressure.

in the ringing traces of Figure 31, the voltage may be computed from the e-folding time of the ringing (in this case, 7 cycles). This works out to a mean resistance of 0.04Ω and, at 22 kA, a mean voltage drop of 900 V. This is consistent with having an XFD in each of the two tube sections running in series. Were the discharge to run longer, it would be expected to transition from the XFD into the hybrid hollow cathode mode at a lower voltage and eventually to an arc.

12. Repetition Rate

The device was run at 1327 Hz and about 20 kV (Figure 32) using a $1.85-\Omega$ load. The average current was 4.4 A, and the E_{bb} was 8 kV. The magnetic pulser output power was 1.4 kW, or 1.6 J per pulse. The input power to the resonantly charged magnetic drive circuit was 440 V at 10 Adc, or 4.4 kW. At frequencies above about 600 Hz, it was difficult to keep the jitter within reasonable bounds. Furthermore, the pulse wave shape tends to smooth out at higher frequencies as though the pressure were low. In fact, the external gauge pressure exceeded the Paschen breakdown limit in several cases (without a breakdown) while the device was running at high frequency. This suggests that the high discharge temperature drives the gas out of the tube into the vacuum station plumbing. No attempt was made to correct this (e.g., by using a differentially pumped gas flow system).

13. Interruption and Pulse Charging Control

In Figure 32 it is evident that the 20-kV PFN voltage was more than twice the 8-kV E_{bb} of the dc power supply. Also, the PFN voltage does not recharge until after the magnetic field pulse has ended. The magnetic field pulse shape was arbitrarily set to be 400 μ sec wide. This meant that, following the discharge of the PFN, the CFCS was still in its on-state for a period (Δt) of about 200 μ sec. Thus, the charging inductor was effectively shorted for a fraction of the normal resonant recharge time (T) of the PFN. This disrupted the normal

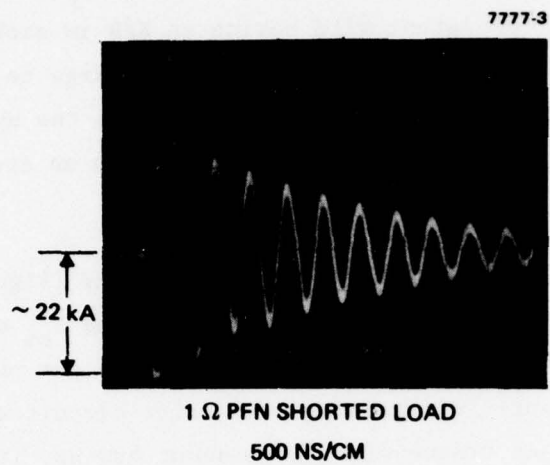


Figure 31. Ringing mode anode current.

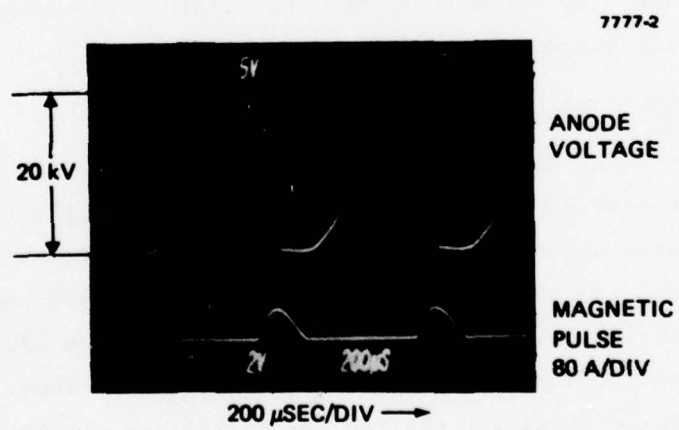


Figure 32. 1327-Hz operation.

phasing of the resonant network and allowed the inductor to be carrying a current ($I = E_{bb} \Delta t / L$) at the time the CFCS interrupted, but with the PFN voltage still zero.

An analysis of this situation shows that the final PFN voltage is given by

$$V = E_{bb} \left[1 + \sqrt{1 + \left(\frac{\pi \Delta t}{T} \right)^2} \right].$$

This may be relevant for future applications. Since Δt can be adjusted at will, the modulator voltage can be adjusted without changing the power supply setting. Since the conduction voltage is low (~ 300 V), the net dissipation would normally be negligible relative to the pulsed phase. (The instantaneous interrupt capability of the CFCS is estimated to be a few kiloamperes at about 10 kV with the grid allowed to float to anode potential.)

14. Jitter

As noted above, there are many sources of jitter: fluctuations in anode voltage, variations in the magnetic field, changes in grid trigger timing, and unstable gas density. Without controlling the pressure, we were able to achieve a jitter time of 10 nsec for over 700 sequential pulses. The theoretical base appears to be sufficient to calculate the jitter for a given system. With care and a set of operating parameters, stable operation would be reproducible.

15. Voltage Holdoff

The voltage holdoff of a CFCS is determined by three factors. The vacuum breakdown potential is nearly proportional to the electrode spacing (d). By contrast, the Paschen breakdown potential is a strongly nonlinearly decreasing function of the pressure multiplied by the spacing (Pd). These two factors determine the optimal spacing for a given pressure. The anode fall time is also a decreasing function of the

pressure (theoretically, the ionization rate is proportional to the gas density). Therefore, the maximum voltage holdoff is ultimately limited by the maximum allowed anode fall time. This limit is complicated by the empirical observation of a deviation from the theoretical variation of anode fall time at low pressure. The deviation is related to earlier observations of an anomalous high-voltage glow discharge at low pressures. In the case of CFCS-T-4, the voltage limit at 1- μ sec rise times is about 60 kV, while at 10 to 50 nsec the voltage must be reduced to about 20 kV.

SECTION 3

THEORETICAL ANALYSIS

A. ANODE FALL CHARACTERISTICS

1. The Trigger

The CFCS uses a slotted cylindrical grid as a trigger electrode. With the grid at the cathode potential and high voltage on the anode, the magnetic field is turned on. Before the magnetic field reaches the magnetic triggering level (V_c), the grid is pulsed to a few kilovolts, and an XFD ignites in the grid-cathode gap. This discharge is only weakly sensitive to the anode voltage and will start at relatively modest magnetic fields.

A fraction of the resulting plasma penetrates through the 21% open area of the grid into the anode space. This fraction may be computed from first principles by the use of detailed balancing. For our present purposes, we assume that it is on the order of the grid current and that a flux of electrons reaches the anode carrying a current of about 50 A. If this current (together with the small increases in the grid voltage during trigger conduction) reduces the anode-grid voltage below V_e , then an XFD will start in the anode region, and the tube will switch on.

2. Inductive Effects

We assume that the effect of the grid is to inject an initial anode current I_o . If the effects of the tube stray capacitance and lead inductance are also considered, then a criterion for proper triggering can be derived. Referring to Figure 33, a low-impedance voltage source V_o is connected to the CFCS. The anode voltage V is initially equal to V_o . When the injected current I_o is turned on, the voltage V falls according to

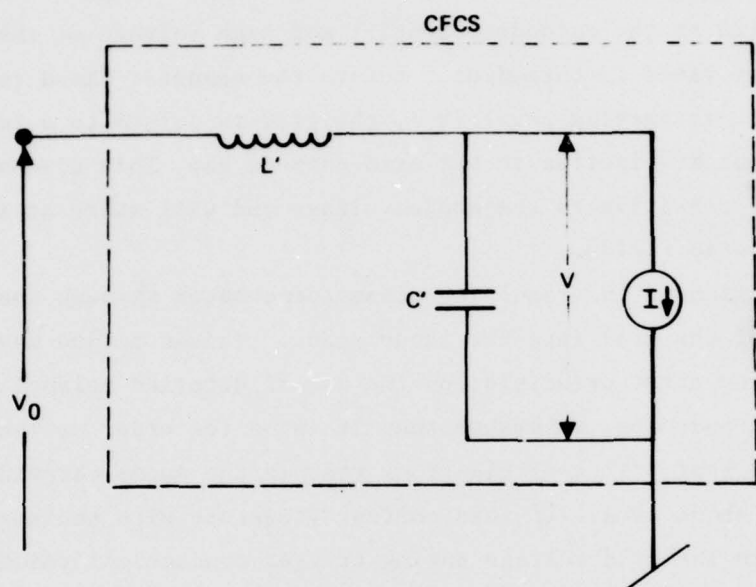


Figure 33. CFCS equivalent circuit.

$$V = V_o - \sqrt{\frac{L'}{C'}} I_o \sin(t/\sqrt{L'C'}). \quad (1)$$

The minimum value of V is then $V_o - \sqrt{\frac{L'}{C'}} I_o$.

If this is below V_c , an avalanche growth of the anode current can begin. This criterion may be written as

$$I_o > (V_o - V_c) \sqrt{\frac{C'}{L'}}. \quad (2)$$

The competition between growth and decay at this critical phase is complicated.

An example of this effect is shown in Figure 34. The initial voltage was 10% higher than the critical voltage. Two values of the initial current were chosen, and the current was assumed to change thereafter according to the growth and decay criteria:

$$\begin{aligned} \dot{I} &= -\Gamma I & V > V_c \\ &= \Gamma I & V \leq V_c, \end{aligned} \quad (3)$$

where

$$\Gamma \approx 9.26 \times 10^9 V^{-0.415} \text{ sec}^{-1}.$$

Obviously, a threshold trigger current exists for ignition to occur. In this case, it is between 50 and 60 A. In the 50-A case, even though the voltage dips below V_c on the second oscillation, the current has decayed too far to grow back up in time to stop the oscillation. Hence, it never goes into full conduction. In the 60-A case, the voltage fall proceeds down to small values.

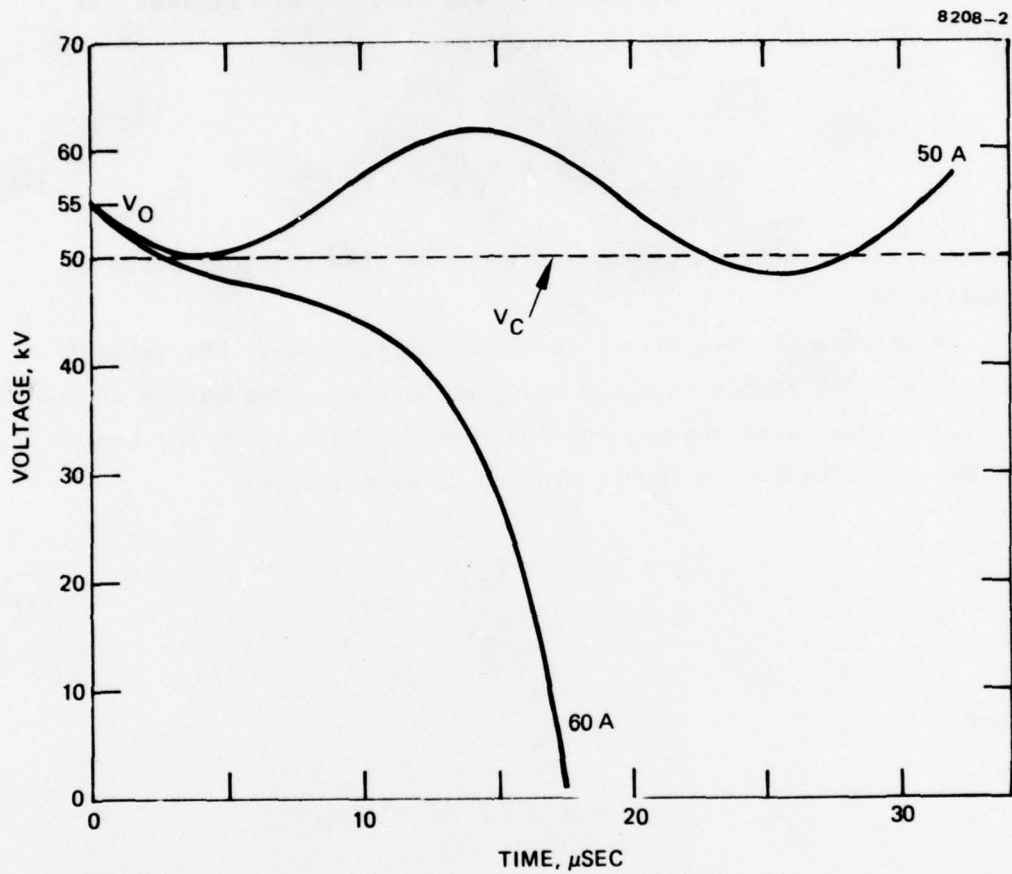


Figure 34. Anode fall (avalanche).
 $L' = 1 \mu\text{H}$ $C' = 50 \text{ pF}$
 $\Gamma = 9.26 \times 10^9 \text{ V}^{-0.415} \text{ sec}^{-1}$

3. Avalanche Growth Rate

The avalanche growth rate Γ has been computed from the known elementary processes. A detailed description of the calculation is beyond the scope of this report. The result is

$$\Gamma = \Gamma_i \left[1 + \gamma e^{-\Gamma_i \left(\frac{Md^2 \xi}{eV_c} \right)^{1/2}} \right], \quad (4)$$

where

$\Gamma_i \equiv \overline{\sigma nv} \equiv$ mean ionization rate averaged over trajectory

$$\approx 6.95 \times 10^{-13} n \cdot (V_c/V)^{0.389}$$

$n =$ neutral helium density (m^{-3})

$M =$ ion mass (kg)

$d =$ gap spacing (0.015 m)

$\xi =$ 0.414 (a geometrical correction factor)

$V_c =$ critical voltage (proportional to B^2)

$\gamma =$ secondary emission coefficient.

For voltages in the ranges of interest,

$$\gamma \approx (V/10,000)^{1/2}, \quad (5)$$

and Γ reduces to the approximate value

$$\Gamma = 9.26 \times 10^9 \cdot N \left(\frac{V_c}{50,000} \right)^{0.389} V^{-0.415} \text{sec}^{-1}. \quad (6)$$

When connected to a PFN and a matched load (and neglecting the inductive effects), the resulting anode fall, shown in Figure 35, is similar to that of Figure 34. The trigger current criterion becomes

$$I_o > \frac{(V_o - V_c)}{2R}, \quad (7)$$

where R is the PFN impedance.

4. Space Charge Limiting

The analysis of the conduction during the anode fall in an XFD at the space-charge limit is considered here only heuristically. To increase the discharge current, a cathode sheath must form whose thickness reduces with time. A consideration of the dynamics of the sheath's motion shows that the velocity of the sheath must approach the speed of an ion with about 200 eV of energy. Therefore, a gradient in the plasma potential must exist to draw these ions from the plasma. This distortion from the steady-state potential distribution would be expected to decrease the normal plasma response time by utilizing secondary electrons to perform some of the ionization. At higher pressures, the net growth rate Γ will approach about half of the avalanche rate calculated in the last section.

5. Conclusions

As higher switching speeds are required, the circuit inductance must be reduced. This must be compensated for by increasing the magnetic field to nearer the critical XFD level, V_c , and by increasing the grid pulse amplitude.

B. SYSTEM STABILITY

1. Jitter

At low pressure, the response of the anode to the magnetic field is slow. This allows the magnetic field to be transiently increased

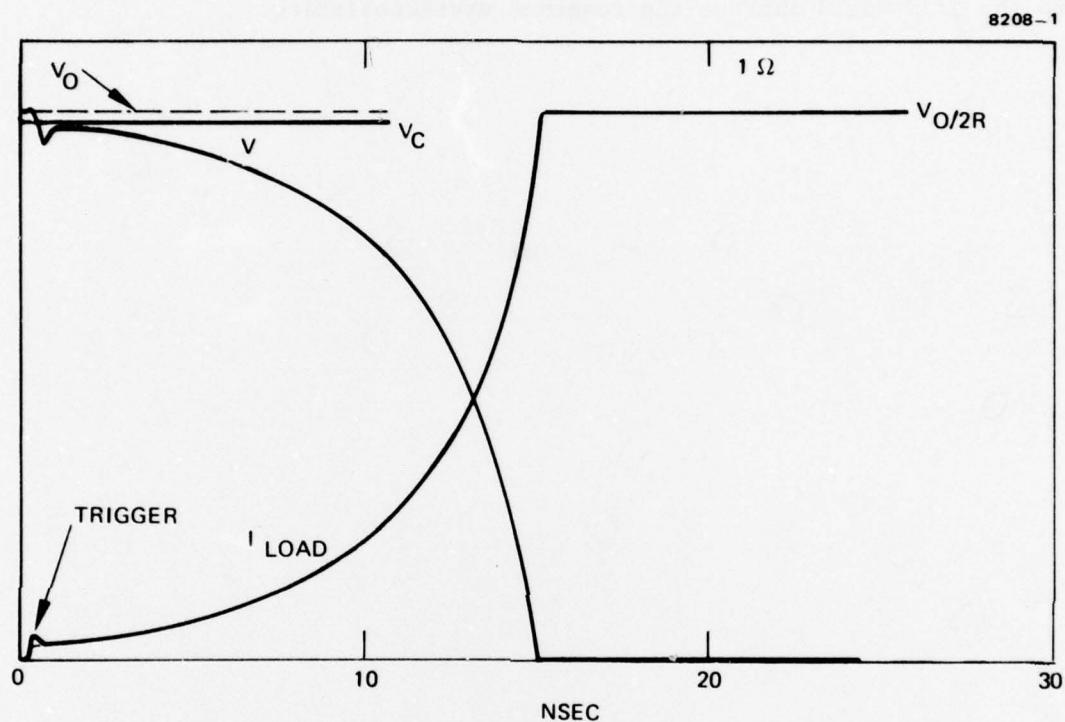


Figure 35. Predicted response to PFN-load circuit assuming no stray L.

substantially beyond V_c before the anode fall occurs. Triggering the grid just before this time can be expected to produce a low jitter level. As the pressure is increased, the formative and statistical time delays are reduced, leading to a greater sensitivity to system fluctuation. In all cases, it appears likely that a low-level sustainer discharge to the grid would improve the response characteristics.

SECTION 4
SUMMARY AND DISCUSSION

The function of the CFCS has been studied over a wide range of variables. It appears that the switch behavior is more complicated than originally expected. Three different modes of conduction have been observed: the conventional XFD, a hybrid hollow-cathode discharge, and vacuum arcs. Depending on the amplitude and duration of the current, conduction may typically pass through these modes in the above sequence.

The CFCS may be triggered magnetically or by grid control into a number of states with varying levels of voltage drop. Conduction may be allowed in the reverse direction or prevented. The present design is limited in response speed and repetition rate by the inductance of the grid and anode leads, the lack of efficient pressure control, and the need for a pulsed magnetic field.

On the basis of the present results, one may conceptually extrapolate towards more advanced switch designs in which these limitations would be overcome. The nature of the design is likely to be a strong function of the application. Although it was pushed harder in several directions, CFCS T-4 appears to have been optimally designed to handle roughly 1 MW of average power for periods to 1 min at 120 Hz with 1- μ sec rise times. The design of a CFCS for shorter rise time pulses would involve modifications of the feed-in configurations, the grid spacings, and the grid pulse waveform. Higher frequencies would require more sophisticated pressure control. Higher voltage would require introducing additional gradient grid structures. Higher peak current is achievable without modification but with a possible reduction in lifetime (presently $\gg 10^6$ pulses). Electrode wear, inverse conduction, and rapid recovery do not seem to pose problems for the CFCS, and extensive electrode conditioning is not essential for normal operation. Taken in total, the CFCS is potentially capable of performing many functions more reliably or effectively than conventional switching devices, and variants of the device may eventually be capable of performing functions not presently achievable by any means.

REFERENCES

1. R.E.B. Makinson, J.M. Somerville, K.R. Makinson, and P. Thoneman, "Magnetically-Controlled Gas Discharge Tubes," JAP 17, p. 567, July 1946.
2. G. Boucher and O. Doebler, "The Artatron - A High-Power Switching Device," 3rd Symposium on Engineering Problems in Thermo-nuclear Research, Munich, June 22-24, 1964.
3. M.A. Lutz, "The Glow-to-Arc Transition - A Critical Review," IEEE Trans. on Plasma Science PS-2, 1, p. 1, March 1974.
4. M.A. Lutz and G.A. Hofmann, "The Gamitron - A High Power Crossed-Field Switch Tube for HVDC Interruption," IEEE Trans. on Plasma Science PS-2, 1, p. 11, March 1974.
5. M.A. Lutz, R.J. Harvey, and H. Alting-Mees, "Feasibility of a High Average Power Crossed Field Closing Switch," IEEE Trans. on Plasma Science PS-4, 2, June 1976.
6. M.A. Lutz, "Gridded Crossed Field Tube," IEEE Trans. on Plasma Science PS-5, 4, p. 24, December 1977.
7. M.A. Lutz, U.S. Patent No. 4034260, July 5 1977.
8. M.A. Lutz and R.J. Harvey, U.S. Patent No. 4034261, July 5, 1977.
9. A.I. Vishnevskii et al., Inst. and Exp. Tech. 14, 3, May 1971 and Pribory i Technika Eksperimenta, No. 5, p. 104, Sept. 1973.
10. A.I. Soldatenko et al., ibid, p. 177.
11. R.J. Harvey, R.W. Holly, and J.E. Creedon, "High Average Power Tests of a Crossed Field Closing Switch," IEEE Publication No. 76CH1147-8, Proc. Int. Pulsed Power Conf. Texas Tech. University, November 9-11, 1976.
12. R.J. Harvey and M.A. Lutz, "High Voltage Ignition of a Crossed Field Discharge," Proc. 12th Int. Conf. on Phenomena in Ionized Gases, Part 1, p. 88, Eindhoven, August 18-22, 1975. North-Holland, N.Y., 1975.
13. B. Wright, 13th Pulse Power Modulator Symposium, Buffalo, N.Y., June 20, 1978.

DISTRIBUTION LIST

012	Defense Documentation Center ATTN: DDC-TCA Cameron Station (Bldg 5) Alexandria, VA 22314	001	Command, Control & Communications Division Development Center Marine Corps Develop & Educ Comd Quantico, VA 22134
001	Code R123, Tech Library DCA Defense Comm Engrg Ctr 1800 Wiehle Ave Reston, VA 22090	001	Rome Air Development Center ATTN: Documents Library (TILD) Griffiss AFB, NY 13441
001	Defense Communications Ag Technical Library Center Code 205 (P.A. Tolovi) Washington, DC 20305	001	HQ, Air Force Systems Command ATTN: DLCA Andrews AFB Washington, DC 20331
001	Office of Naval Research Code 427 Arlington, VA 22217	001	Cdr, MIRANCOM Redstone Scientific Info Center ATTN: Ch, Document Section Redstone Arsenal, AL 35809
001	Commander Naval Surface Weapons Center Attn: F-12 (K. Baile) Dahlgren, VA 22448	001	Commandant US Army Aviation Center ATTN: ATZQ-D-MA Fort Rucker, AL 36362
001	Cdr, Naval Surface Weapons Cen White Oak Laboratory ATTN: Library Code WX 21 Silver Spring, MD 20910	001	Director, Ballistic Missile Defense Advanced Technology Center ATTN: ATC-R, PO Box 1500 Huntsville, AL 35807
001	Commander Naval Surface Weapons Center ATTN: Dr. M. F. Rose Dahlgren, VA 22448	001	Commander US Army Intelligence Center & School ATTN: ATSI-CD-MD Fort Huachuca, AZ 85613
001	Commander Naval Surface Weapons Center ATTN: Dr. Gripshover Dahlgren, VA 22448	001	Commander HQ, Fort Huachuca ATTN: Technical Reference Div Fort Huachuca, AZ 85613
001	Commander Naval Surface Weapons Center ATTN: F-12 (D. Lindberg) Dahlgren, VA 22448	001	Commander Naval Surface Weapons Center ATTN: F-12 (H. Odom) Dahlgren, VA 22448

001 Director
Naval Research Laboratory
ATTN: Code 2627
Washington, DC 20375

001 Deputy for Science & Technology
Office, Assist Sec Army (R&D)
Washington, DC 20310

001 HQDA (DAMA-ARZ-D/Dr. Verderame)
Washington, DC 20310

001 Commandant
US Army Signal School
ATTN: ATSN-CTD-MS
Fort Gordon, GA 30905

001 Cdr, Harry Diamond Labs
ATTN: Library
2800 Powder Mill Road
Adelphi, MD 20783

001 Director
US Army Ballistic Research Labs
ATTN: DRXBR-LB
Aberdeen Proving Ground, MD 21005

001 Harry Diamond Laboratories, DA
ATTN: DELHD-RCB (Dr. Nemarich)
2800 Powder Mill Road
Adelphi, MD 20783

001 Director, US Army Materiel
Systems Analysis Activity
ATTN: DRXSY-T
Aberdeen Proving Ground, MD 21005

001 Mr. A. Gordon
ITT Electron Tube Division
Box 100
Easton, PA 18042

001 Mr. Dave Turnquist
EG&G, Inc
35 Congress Street
Salem, MA 01970

001 Cdr, Naval Air Systems Command
NAVAIR-350F (R. J. Wasneski)
Washington, DC 20361

002 Commander, Picatinny Arsenal
ATTN: SARPA-FR-5
Bldg 350
Dover, NJ 07801

001 Commander
US Army Satellite Communications
Agency
ATTN: DRCPM-SC-3
Fort Monmouth, NJ 07703

001 CDR, USA Missile R&D Command
ATTN: DRCPM-HEL (T. Roberts)
Redstone Arsenal, AL 35809

001 Cdr, Rome Air Development Center
ATTN: Mr. B. Gray
Griffis AFB, NY 13441

001 Cdr, Ballistic Missile Defense
Advanced Technology Center
ATTN: ATC-T (L. Havard)
Redstone Arsenal, AL 35809

001 Cdr, US Army Mobility Equipment
Research & Development Command
ATTN: DRDME-EA (Dr. Amstutz)
Fort Belvoir, VA 22060

001 Cdr, Naval Surface Weapons Center
ATTN: Mr. C. Hudelson
White Oak Laboratory
Silver Spring, MD 20910

001 Cdr, Air Force Aero Propulsion Lab.
AFAPL/POD-1 (Mr. R. Verga)
Wright-Patterson AFB, Ohio 45433

001 Dr. S. A. Gilmore
Dept of Electrical Engineering
State University of New York
4232 Ridge Lea Road
Amherst, NY 14226

001 Dr. M. Kristiansen
Texas Tech University
College of Engineering
PO Box 4439
Lubbock, Texas 79409

001	Cdr, US Army Research Office ATTN: DRXRO-IP PO Box 12211 Research Triangle Park, NC 27709	002	Commander US Army Logistics Center ATTN: ATCL-MC Fort Lee, VA 22801
001	Cdr, US Army Research Office ATTN: DRXRO-PH (Dr. R. Lontz) PO Box 12211 Research Triangle Park, NC 27709	001	Cdr, PM Concept Analysis Center ATTN: DRCPM-CAC Arlington Hall Station Arlington, VA 22212
001	Commandant US Army Inst for Military Assistance ATTN: ATSU-CTD-MO Fort Bragg, NC 28307	001	Chief Ofc of Missile Electronic Warfare Electronic Warfare Lab, ERADCOM White Sands Missile Range, NM 88002
001	Commandant US Army Air Defense School ATTN: ATSA-CD-MC Fort Bliss, TX 79916	001	Chief Intel Materiel Dev & Support Ofc Electronic Warfare Lab, ERADCOM Fort Meade, MD 20755
001	Commander US Army Nuclear & Chemical Agency 7500 Backlick Rd, Bldg 2073 Springfield, VA 22150	001	Cdr, Harry Diamond Labs ATTN: DELHD-CO 2800 Powder Mill Road Adelphi, MD 20783
001	Hq, TCATA Technical Information Center ATTN: Mrs. Ruth Reynolds Fort Hood, TX 76544	001	Commander ARRADCOM DRDAR-TSB-S Aberdeen Proving Ground, MD 21005
001	Commander, DARCOM ATTN: DRCDE 5001 Eisenhower Ave Alexandria, VA 22333	001	Commander, ERADCOM ATTN: DRDEL-CG; -CD: -CS (IN TURN) 2800 Powder Mill Road Adelphi, MD 20783
001	Cdr, US Army Signals Warfare Lab ATTN: DELSW-OS Vint Hill Farms Station Warrenton, VA 22186	001	Cdr, ERADCOM ATTN: DRDEL-CT 2800 Powder Mill Road Adelphi, MD 20783
001	Commander US Army Mobility Equip. R&D Command ATTN: DRDME-R Fort Belvoir, VA 22060	001	Dr. John Hammond W. J. Schafer Associates, Inc. Clinton Bldg, Suite 408 2109 W. Clinton Avenue Huntsville, AL 35805
001	Maxwell Laboratories ATTN: Mr. R. Fitch 9244 Balboa Ave. San Diego, CA 92123	001	Cdr, Air Force Weapons Laboratory AFWL/ALE (J. O'Loughlin) Kirtland Air Force Base New Mexico 87117

001	CDR, ERADCOM ATTN: DRDEL-PAO 2800 Powder Mill Road Adelphi, MD 20783	Commander US Army Communications & Electronics Materiel Readiness Command Fort Monmouth, NJ 07703
001	CDR, ERADCOM ATTN: DRDEL-LL; -SB; -AP (IN TURN) 2800 Powder Mill Road Adelphi, MD 20783	1 DRSEL-PL-ST 1 DRSEL-MA-MP 2 DRSEL-PA
001	Cdr, ERADCOM ATTN: DRDEL-AQ 2800 Powder Mill Road Adelphi, MD 20783	001 CINDAS Purdue Industrial Research Park 2595 Yeager Road W. Lafayette, IN 47096
001	CDR, ERADCOM ATTN: DRDEL-PA; -ILS; -ED (IN TURN) 2800 Powder Mill Road Adelphi, MD 20783	002 MIT - Lincoln Laboratory ATTN: LIBRARY (Rm A-082) PO Box 73 Lexington, MA 02173
001	Hqs, Harry Diamond Laboratories ATTN: DELHD-TD (Dr. W.W.Carter) 2800 Powder Mill Road Adelphi, MD 20783	001 NASA Scientific & Tech Info Facility Baltimore/Washington Intl Airport PO Box 8757, MD 21240
<p>Commander US Army Electronics R&D Command Fort Monmouth, NJ 07703</p> <ul style="list-style-type: none"> 1 DELET-D 1 DELET-DD 2 DELET-DT 5 DELET-BG 1 DELSD-L (Tech Library) 2 DELSD-L-S (STINFO) 		
<p>Commander US Army Communications R&D Command Fort Monmouth, NJ 07703</p> <ul style="list-style-type: none"> 1 DRDCOM-COM-RO 1 USMC-LNO 1 ATFE-LO-EC 		
001	Cdr, Air Force Weapons Laboratory ATTN: Dr. A. Guenther (AFWL/CA) Kirtland Air Force Base, NM 87117	001 TACTEC Batelle Memorial Institute 505 King Avenue Columbus, OH 43201
001	Lawrence Livermore Laboratory ATTN: L. Reginato PO Box 808 Livermore, CA 94550	001 Plastics Tech Eval Center Picatinny Arsenal, Bldg 176 ATTN: MR. A.M. Anzalone Dover, NJ 07801
		001 Metals & Ceramics Inf Center Batelle 505 King Avenue Columbus, OH 43201

001 Mr. Phil Mace
Los Alamos Scientific Laboratory
PO Box 1663
Los Alamos, NM 87545

001 Avco-Everett Research Laboratory
2385 Revere Beach Parkway
ATTN: Mr. R. Feinberg
Everett, MA 02149

001 Cdr, Defense Advanced Research
Project Agency
DARPA/STO (J. Mangano)
1400 Wilson Boulevard
Arlington, VA 22209